TESIS – MM2341

Sintesis WO_3 menggunakan Metode Hidrotermal sebagai Material Anoda Baterai Ion Lithium dengan Kapasitas Balik dan Stabilitas Siklus yang Tinggi

AUGUS TINO TRI WIDYANTORO
NRP. 2712 201 905

Dosen Pembimbing:
Diah Susanti, ST., MT., Ph.D
Prof. Chen-Hao Wang

PROGRAM MAGISTER
BIDANG KEAHLIAN MATERIAL INOVATIF
TEKNIK MATERIAL DAN METALURGI
Fakultas Teknologi Industri
Institut Teknologi Sepuluh Nopember
Surabaya
2014

(This page is empty deliberately)

THESIS – MM2341

Synthesis of WO_3 via Hydrothermal Method with Improved Reversible Capacity and Cyclic Stability as Anode Material for Lithium-Ion Batteries

AUGUS TINO TRI WIDYANTORO
NRP. 2712 201 905

Advisor:
Diah Susanti, ST., MT., Ph.D
Prof. Chen-Hao Wang

MASTER DEGREE PROGRAM
EXPERTISE AREA OF INNOVATIVE MATERIALS
DEPARTMENT OF MATERIALS AND METALLURGICAL ENGINEERING
Faculty of Industrial Technology
Sepuluh Nopember Institute of Technology
Surabaya Indonesia
2014

(This page is empty deliberately)

Sintesis WO_3 menggunakan Metode Hidrotermal sebagai Material Anoda Baterai Ion Lithium dengan Kapasitas Balik dan Stabilitas Siklus yang Tinggi

LAPORAN TESIS
Diajukan untuk memenuhi salah satu syarat memperoleh
Gelar Magister Teknik (M.T.) pada Bidang Studi Material Inovatif
Program Studi Magister Teknik Material dan Metalurgi
FTI-ITS

Oleh:
Augus Tino Tri Widyantoro
NRP : 2712 2019 05

Telah disidangkan pada:

Hari : Jum'at
Tanggal : 18 Juli 2014
Tempat : Ruang MTL 345 Jurusan Teknik Material dan Metalurgi FTI-ITS

Mengetahui/menyetujui:

Dosen Penguji

1. Dr. Hosta Ardhyananta, S.T., M.Sc
   NIP. 198012072005011004

2. Lukman Noerochim, S.T., M.Sc.Eng., Ph.D.
   NIP. 197703132003121001

3. Dr. Widyastuti, S.Si, M.Si.
   NIP. 197906202006042001

Dosen Pembimbing

Diah Susanti, S.T., M.T., Ph.D.
NIP. 197701162003122001

Direktur Program Pascasarjana

Prof.Dr.Ir. Adi Soeprijanto, MT.
NIP. 196404051990021001

Sintesis WO_3 menggunakan Metode Hidrotermal sebagai Material Anoda Baterai Ion Lithium dengan Kapasitas Balik dan Stabilitas Siklus yang Tinggi

Nama Mahasiswa : Augus Tino Tri Widyantoro
NRP : 2712 201 905
Dosen Pembimbing : (a) Diah Susanti, ST., MT., Ph.D
(b) Prof. Chen-Hao Wang

ABSTRAK

Tungsten trioksida memiliki prospek yang bagus untuk dijadikan material anoda baterai ion lithium karena temperatur leleh yang tinggi, stabilitas mekanik yang tinggi, biaya rendah, kapasitas teoritis dan volumetrik yang besar. Tujuan penelitian ini adalah untuk memperkenalkan material anoda baru dengan performa yang tinggi sebagai pengganti grafit pada baterai ion lithium. Heksagonal WO_3 telah disintesis menggunakan metode hidrotermal dan kemudian material tersebut dievaluasi sebagai material anoda untuk baterai ion lithium. Rasio molar $Na_2WO_4.2H_2O$/Na-EDTA dan temperatur reaksi diketahui mempunyai peranan penting terhadap morfologi dan sifat elektrokimia dari produk WO_3.

Morfologi WO_3 tanpa penambahan NaCl atau Na-EDTA (WO_H180T20) adalah nanopartikel, sedangkan morfologi WO_3 dengan penambahan NaCl dan Na-EDTA yang disintesis pada temperatur 210^oC (WO_H210T20_CE0.8) adalah *rod like structure.* WO_H180T20 mempunyai kapasitas discharge awal sebesar 814.3 mAh/g dengan efisiensi pertama sebesar 53.7%. Di sisi lain, WO_H210T20_CE0.8 mempunyai performa elektrokimia yang bagus dengan kapasitas discharge awal 558.9 mAh/g dan effisiensi pertama sebesar 86.9%.

Hal ini membuktikan bahwa h-WO_3 adalah salah satu kandidat material yang potensial untuk anoda baterai ion lithium. Peningkatan performa elektrokimia WO_3 dapat disebabkan oleh struktur morfologi yang teratur. Na-EDTA tidak hanya diketahui berpengaruh pada keseragaman dan kekristalan yang tinggi pada produk, tetapi juga berperan penting dalam perilaku pertumbuhan WO_3 selama proses sintesis.

Nanokomposit tungsten trioksida/reduced grafena oksida (WO_3/rGO) juga telah disintesis dengan menggunakan metode hidrotermal dan dievaluasi sebagai material anoda untuk baterai ion lithium. Pada siklus yang pertama, elektroda nanokomposit (WO_H180T20_GO8%) mengasilkan kapasitas discharge sebesar 987.4 mAh/g dengan efisiensi sebesar 64.6%. Selain itu, pada densitas arus 700 mA/g, elektroda ini mampu menghasilkan kapasitas sebesar 219.5 mAh/g setelah 100 siklus. Peningkatan performa elektrokimia pada material ini dapat disebabkan oleh kombinasi struktur yang unik antara WO_3 dan rGO.

Kata kunci: Tungsten trioksida, material anoda, baterai ion lithium, efisiensi.

(This page is empty deliberately)

Synthesis of WO_3 via Hydrothermal Method with Improved Reversible Capacity and Cyclic Stability as Anode Material for Lithium-Ion Batteries

Student Name : Augus Tino Tri Widyantoro
NRP : 2712 201 905
Advisors : (a) Diah Susanti, ST., MT., Ph.D
(b) Prof. Chen-Hao Wang

ABSTRACT

Tungsten trioxide (WO_3) is expected to be profitable in improving of LIBs due to enhanced safety because of high melting temperature and mechanical stability, low cost, large theoretical capacity (693 mAh/g) and high volumetric capacity. The objective of the contribution is to introduce a high performance anode alternative to graphite for lithium-ion batteries. Hexagonal WO_3 was synthesized via hydrothermal route using NaCl and/or Na-EDTA as structure directing templates and then these materials were evaluated as an anode material for lithium ion batteries. The $Na_2WO_4.2H_2O$/Na-EDTA molar ratio and the reaction temperature are found to play important roles in determining the morphologies and electrochemical properties of the WO_3 product.

The morphology of WO_3 product without adding either NaCl or Na-EDTA (WO_H180T20) is nanoparticle whereas that of WO_3 product with adding NaCl and Na-EDTA synthesized at 210^{o}C (WO_H210T20_CE0.8) is rod like structure. WO_H180T20 has initial discharge capacity of 814.3 mAh/g with a first coulombic efficiency of 53.7%. On the other hand, WO_H210T20_CE0.8 has a good electrochemical performance with initial discharge capacity of 558.9 mAh/g and a high first coulombic efficiency of 86.9 %. These proved that h-WO_3 is one of good candidate materials for lithium ion battery anode. The improved electrochemical performance of WO_3 could be ascribed to the highly ordered self-assemble structures. Na-EDTA is not only found to be responsible for the especially good uniformity and high crystallinity of the products, but also play important role in restricting the natural growing habit of WO_3 due to the possible selective interaction between EDTA and certain crystal facets, thus having a great impact over its final morphology.

Tungsten trioxide/reduced graphene oxide (WO_3/rGO) nanocomposites also were synthesized via hydrothermal method and evaluated as an anode material for lithium batteries. At first cycle the nanocomposite electrode (WO_H180T20_GO8%) exhibits a discharge capacity of 987.4 mAh/g with a coloumbic efficiency of 64.6%. And at a current density of 700 mA/g it can delivers as high as 219.5 mAh/g after 100 cycles. The improved electrochemical performance could be attributed to the incorporation of rGO and the unique structure of the nanocomposite.

Keywords: Tungsten trioxide, anode materials, lithium ion batteries, coulombic efficiency

(This page is empty deliberately)

PREFACE

Segala puji bagi Allah سبحانه وتعالى yang maha pengasih lagi penyayang, Rabb yang maha menguasai segala ilmu dan kalam. Shalawat dan salam semoga selalu tercurah kepada Rasulullah Muhammad صلى الله عليه وسلم yang telah menuntun kita kepada jalan kebenaran dan menjadi suri tauladan yang baik.

Saya ingin mengucapkan terimakasih yang sedalam dalamnya untuk Ibu dan Bapak saya atas kasih sayang dan do'a yang selalu di panjatkan untuk saya, tanpa ridho mereka saya tidak akan bisa sampai seperti sekarang ini. Terimakasih juga kepada kakak-kakak saya, mb Yanti dan mas Anto sekeluarga, yang selalu mendukung saya.

Special thanks to my supervisor, Prof. Chen-Hao Wang for his support during these a year, and my co-advisor, Dr. Ming-Yao Cheng (Dr. Matt) and Prof. Bing-Joe Hwang, who always teach me patiently how to conduct experiment and write a report in a very good way. I got a lot of experience from them.

I would like to acknowledge bu Diah Susanti, Ph.D, for making possible I got studied at ITS Surabaya and NTUST, Taiwan.

Last but not least I would like to thank to Hanif and Erik (terimakasih atas bantuannya selama saya di ITS), mb Nikmah (terimakasih atas nasehatnya), Vuri (ayo pulang kampung!), Melissa (thanks for your kindly cooperation and assistances), my roommates at Padepokan 212 yang selalu asyik dan rame (Alvin, Kevin, Peter and Tri), LiBs group members (Sunny, Wayne, Kurt, Nathen, david, Bill, Jill, Ase, Ate), E2-518 lab members (Hogie, Hoa, Kha, Thanh, Steven, Hakun, Benjen, Kha, Mark, Ryker, Sui, Mawan, Demi, Belete, Amare, Andy, Cindy, Doris, Ethan, Anny), E1-133 lab members (Wei-Ting Tsao, Kai-Chin Wang, Bing-Yuan Yao, Yu-Chen Shih, Y u-Chuan Lin, Chang-Hui Lin, Nguyenanh Thu, Sun-Tang Chang, Hsin-Cheng Hsu, Hsin-Chih Huang, Kuan-Cheng Chen, Yu-Chung Chang, Chung-Ta Chang) and all of my friends from Indonesia that I can not mention one by one. Thank you for all of your help and kindness. You all guys teach me about life, not only explicit but also implicit.

(This page is empty deliberately)

TABLE OF CONTENTS

(This page is empty deliberately)

ILUSTRATION

(This page is empty deliberately)

LIST OF TABLES

(This page is empty deliberately)

CHAPTER 1
INTRODUCTION

1.1 Research Background

Lithium-ion batteries play a significant role as energy storage devices in the communications, transportation and renewable-energy sectors. Graphite is current choice of anode materials for lithium-ion batteries due to its relatively low cost, abundant material supply and long cycle life. However, the low energy density (375mAh/g) and safety issues related to lithium deposition become disadvantages of graphite(Shukla and Prem Kumar, 2013). Thus, there has been a great challenge in developing alternative anode materials with high energy density, long cycle life, enhanced safety, and low cost (Larcher et al., 2007).

Tungsten oxide (WO_3) has received wide attention owing to its promising application for gas sensors, electrochromic and photochromic devices, secondary batteries, photocatalysts, heterogeneous catalysts, solar energy devices, field electron emission and electrocatalyst (Ham et al., 2010). Hexagonal form of tungsten trioxide (h-WO_3) is of great interest owing to its well-known tunnel structure and a promising material for negative electrodes of rechargeable lithium batteries(Gu et al., 2007).

WO_3 is expected to be profitable in improving of LIBs due to enhanced safety because of high melting temperature and mechanical stability, low cost and large theoretical capacity (~700 mAh/g). More importantly, a very high volumetric capacity can be expected considering its high theoretical density of 7.61 $g\,cm^{-3}$ (Yoon et al., 2011). However, the low 1st coulumbic efficiency and the poor cyclability of this material during the continuous charge/discharge cycling are the main disadvantages that restrained the application of WO_3 as anode material for lithium-ion batteries. This problem is mainly attributed to the formation of solid electrolyte interface layer (Wang et al., 2014).

Although substantial progress has been made in different material system, there is less reports for WO_3 in the field of energy conversion/storage such us Li-Ion battery(Sasidharan et al., 2012). Gu et al., 2007 have prepared hexagonal tungsten trioxide nanowires in a large scale by a simple hydrothermal method

without any templates and catalysts. However it only delivers a low discharge capacity of 218 mAh/ with a coulombic efficiency of 75.6% for the first cycle. Meanwhile an ordered mesoporous WO_{3-x} with high electrical conductivity (m-WO_{3-x}) was prepared by Yoon et al., 2011 as an anode material for lithium ion batteries (LIBs). It exhibits a reversible capacity of 748 mAh/g with 1st coulombic efficiency is only 53%.

Furthermore, Yin et al., 2012 had synthesized γ-WO_3 hierarchical nanostructures by using a biomolecule-assisted hydrothermal approach between $Na_2WO_4 \cdot 2H_2O$ and glycine acid. However it has only discharge capacity of 515.1 mAh/g and coulombic efficiency of 62.4% for the first cycle.

To understand the effect of nanostructure to the elecrochemical performance of WO_3, we investigate the preparation of WO_3 via hydrothermal synthesis under various structure directing agents. Hydrothermal process offers significant advantages in controlling over the product shape and size at low processing temperature, extreme homogeneity, and low cost. NaCl was used as a crystal modifier to control the growth rate of the product and Na-EDTA was used as a chelating ligand and structure-directing agent to produce h-WO_3 nanocrystal. In the last part, rGO was added into WO_3 to improve its electrochemical performance. rGO could not only induce formation of fine particles with uniform dispersion and control its morphology through high chemical functionality, but also shorten lithium ion transporting distance and increase electronic conductivity, then the metal oxides could display longer cycle life and better rate performance.

Subsequently, the structures and morphologies of WO_3 were analyzed by using X-ray Difraction (XRD), Scanning Electron Microscopy (SEM), Thermo gravimetric analysis (TGA) and Raman Spectroscopy. Meanwhile, electrochemical properties were analyzed by using galvanostatic charge-discharge and cyclic voltammetry.

1.2 Research Objectives

The objectives of this work are to:

a. Study the effect of sodium salts as structure directing agents on the morphologies and electrochemical performances of WO_3.
b. Study the effect of reaction temperature on the morphologies and electrochemical performances of WO_3.
c. Study the effect of Na-EDTA molar ratio on the morphologies and electrochemical performances of WO_3.
d. Study the effect of GO weight ratio on the morphologies and electrochemical performances of WO_3.

1.3 Research Advantages

This work is expected to produce WO_3 that can be applied as anode material for lithium ion battery which has a high capacity, high reversible capacity, high capacity retention and long cycle life.

(This page is empty deliberately)

CHAPTER 2
LITERATURE REVIEW

2.1 Lithium Ion Battery Anode

2.1.1 Li-ion cell design and components

There are three main parts of lithium ion batteries: anode, cathode, and electrolyte. Figure 2.1 shows a rough schematic of a lithium ion cell. During discharge, the cathode (typically a lithium metal oxide such as $LiFePO_4$, $LiMn_2O_4$, $Li_3V_2(PO_4)_3$ and $LiCoO_2$) acts as the positive terminal of the battery and the anode (commercially composed of graphitic carbon) acts as the negative terminal. The cathode reacts according to the following half reaction (de las Casas and Li, 2012):

$$LiMO_2 \leftrightarrow Li_{1-x}MO_2 + xLi+ + xe^-$$

Similarly, the anode reacts according to the following half reaction:

$$xLi^+ + xe^- + 6C \leftrightarrow Li_xC_6$$

During charging Li^+ ions move from cathode to anode via electrolyte, whereas during discharging they move reversely. The electrolyte is typically a lithium salt such as $LiPF_6$ dissolved in organic solvent (ethylene carbonate and/or diethylene carbonate). Importantly, the electrolyte does not enable the conduction of free electrons; instead, the electrons that complete the half reaction move via an external wire. Commercially, the most common cathode material has been lithium cobalt oxide since its introduction by Sony in the early 1990s, due to its high energy density. Lithium manganese oxide is also commonplace in cathodes where higher current density is a concern (Ohzuku and Brodd, 2007).

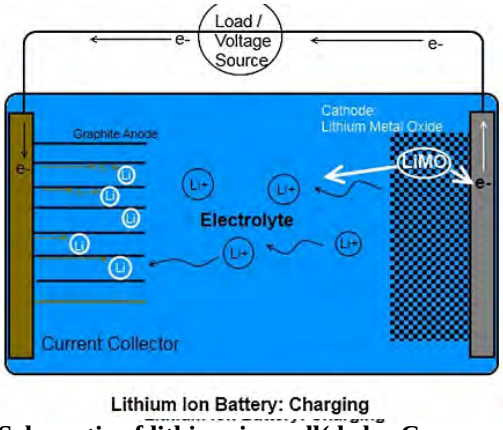

Figure 2.1 Schematic of lithium ion cell(de las Casas and Li, 2012)

Depending on their Li-ion battery performances and reaction mechanism, anode materials could be classified into three groups (Table 2.1):

a) Intercalation/de-intercalation materials, such as carbon based materials, graphene, carbon nanotubes, porous carbon, TiO_2 and $Li_4Ti_5O_{12}$, etc
b) Alloy/de-alloy materials, such as Si, Ge, Sn, Al, Bi, SnO2, etc
c) Conversion materials, such as metal oxide (Mn_xO_y, NiO, Fe_xO_y, CuO, Cu_2O, MoO_2etc.), metal sulphides, metal phosphides and metal nitrides (M_xX_y; here X = S, P, N)(Goriparti et al., 2014).

Table 2.1 Most common anode materials used for lithium ion batteries(Goriparti et al., 2014)

Reaction Mechanism	Active anode material	Advantages	Common issues
Insertion/de-insertion materials	1. Carbonaceous a. Hard carbons b. CNTS c. Graphene 2. Titanium oxides a. $LiTi_4O_5$ b. TiO_2	• Good working potential • Low cost • Good safety • Extreme safety • Good cycle life • Low cost • High power capability	• Low coulombic efficiency • High voltage hysteresis • Very low capacity • Low energy density
Alloy/de-alloy materials	a. Silicon b. Germanium c. Tin d. Antimony e. Tin oxide f. SiO	• Higher specific capacities • High energy density • Good safety	• Large irreversible capacity • Huge capacity fading • Poor cycling
Conversion materials	a. Metal oxides (Fe_2O_3, Fe_3O_4, CoO ,Co_3O_4, Mn_xO_y ,Cu_2O /CuO, NiO, Cr_2O_3,	• High capacity • High energy • Low cost • Environmentally	• Low coulumbic efficiency • Unstable SEI formation

	RuO_2, MoO_2/MoO_3, etc.) b. Metal phoshides/ sulfides/ nitrides (MX_y; M = Fe, Mn, Ni, Cu, Co etc. and X=P, S, N)	compatibility • High specific capacity • Low operation potential and Low • polarization than counter oxide	• Large potential hysteresis • Poor cycle life • Poor capacity retention • Short cycle life • High cost of production

Active materials, in order to be considered suitable candidates for LIBs anode, should fulfil the requirements of reversible capacity, good ionic and electrical conductivity, long cycle life, high rate of lithium diffusion into active material and conclusively low cost and ecocompatibility(Goriparti et al., 2014).

2.1.2 Carbon based anodes

Anodes in many commercial grade lithium ion batteries are composed of graphitic carbons because of their low expansion during lithium insertion. This low expansion is directly linked to their ability to maintain their charge capacity after many charge-discharge cycles. The reasons for this will become clear later, but in any case, their predominance in the market is a result of their cycle over cycle efficiency, not their capacity. When lithium intercalates in graphite, it occupies an interstitial site between two planes of graphite (Figure 2.2). Lithium ions can only combine on every 2nd carbon hexagon in the graphite sheet which limits the amount of lithium ions to 1 for every 6 carbon atom. This is directly linked to the energy storage density of graphite in Li-ion batteries. The lithium insertion capacity of graphite (372 mAh/g) is a relatively low capacity, and lithium ion cells stand to gain much if this value is increased(de las Casas and Li, 2012).

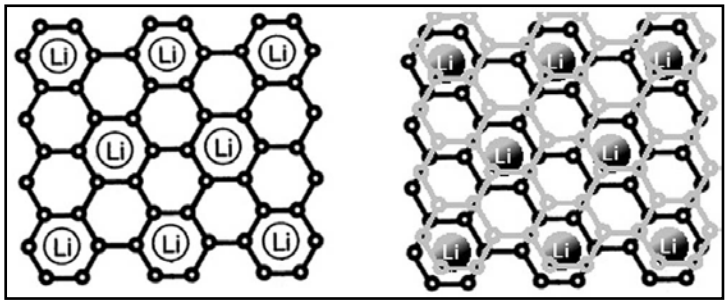

Figure 2.2 Schematic of lithium intercalation in graphite. (a) Lithium is inserted in every 2nd carbon hexagon and (b) between the graphite layer(de las Casas and Li, 2012)

2.1.3 Metal and Alloy based Anodes

There are some metal that have greater capacities that of graphite such as aluminum (993 mAh/g for LiAl and 2234 mAh/g for Al_4Li_9), tin (994 $mAhg^{-1}$ $Li_{22}Sn_5$) and antimony (536 $mAhg^{-1}$ Li_3Sb)(Munshi, 1995). The lithium in these materials is not stored through the intercalation mechanism that graphite uses but they are capable of forming an alloy with metals. By forming alloys, these metals are capable of storing far more lithium per gram than graphitic carbon can. For comparison, whereas it takes 6 carbons in graphite to insert one lithium ion, whereas one aluminum or tin atom can often alloy itself with 2–4 lithium atoms(Munshi, 1995).

This large change in volume, sometimes an expansion/contraction of 500%, causes the structural integrity of the anode to be compromised, which then causes the anode to physically crumble (Obrovac and Christensen, 2004). This process is called pulverization, and is the primary reason that metal alloys are not used in rechargeable batteries. Once pulverization occurs, it cannot be reversed and the battery permanently loses a fraction of its capacity. When a metal alloy based anode is used repeatedly, it results in an exponential decay of capacity. It is evident then, that to improve the capacity of a rechargeable battery such as the lithium ion cell, a simple metal alloy anode will not suffice (de las Casas and Li, 2012).

2.1.4 Conversion based Anodes

There are some transition metal compounds such as oxides, phosphides, sulphides and nitrides (M_xN_y; M=Fe, Co, Cu, Mn, Ni and N=O, P, S and N) which utilized as anodes in LIBs. The electrochemical reaction mechanism

involving these compounds together with lithium, implies the reduction/oxidation of the transition metal along with the composition/decomposition of lithium compounds (Li_xN_y; here N=O, P, S and N). Anodes based on these compounds (included WO_3) exhibit high reversible capacities (500-1000 mAh/g) owing to the participation of a high number of electrons in the conversion reactions. The electrochemical conversions reactions can be described as follows(Goriparti et al., 2014):

$M_xN_y+zLi^++ze^- \leftrightarrow Li_zN_y + xM$ (here M= Fe, Co, Cu, Mn or Ni & N= O, P or N)

2.2 Tungsten Trioxide (WO_3)

Tungsten oxide (WO_x) has received wide attention because it has many application such as gas sensors, electrochromic and photochromic devices, secondary batteries, photocatalysts, heterogeneous catalysts, solar energy devices, field electron emission and electrocatalyst in electrolysis of water for hydrogen production (Ham et al., 2010). Tungsten has many oxidation states, i.e., 2, 3, 4, 5 and 6, thereofore the tungsten compound can exist in many forms. For instance, the typical forms of tungsten oxides are tungsten (VI) oxide: WO_3 (lemon yellow appearance) and tungsten (IV) oxide: WO_2 (brown and blue appearance) (Supothina et al., 2007).

WO_3 with different morphologies such as nanowires, nanorods, nanoplates and nanoparticles were successfully synthesized by various methods, including hydrothermal reaction (Li et al., 2006), thermal oxidization (Siciliano et al., 2008), inorganic–organic hybrid method (Chen et al., 2008), pulsed spray pyrolysis deposition technique (Bathe and Patil, 2009), and wet chemical precipitation (Wolcott et al., 2006). Among them, hydrothermal process offers significant advantages in controlling over the product shape and size at high homogeneity, low cost and low processing temperature by combining with soft templates as chelating ligands and capping reagents, such as ethylene diamine tetraacetate acid (EDTA), polyethylene glycol (PEG) and polyvinyl alcohol (PVA) to produce 1D nanostructure (Ham et al., 2010).

There are some kinds of precursors for large-scale production of WO_3. These can use a variety of different precursors, for example: sodium tungstate hydrate, tungsten oxychloride, tungsten alkoxide, dissolved tungsten metal, tungsten hexachloride, tungsten oxide and hydrated ammonium metatungstate (Baker et al., 2002).

Hexagonal form of tungsten trioxide (Figure 2.3) is of great interest owing to its well-known structural tunnel cavities in which WO_6 octahedrons shared their corners with each other thus forming hexagonal tunnel cavities along c-axis. Among various crystal structures of WO_3, hexagonal tungsten oxide (h-WO_3) was widely investigated, especially as an intercalation host to obtain hexagonal tungsten bronzes M_xWO_3 (M= K^+, Li^+, etc.) and as a promising material as anode material for lithium ion battery (Gu et al., 2007).

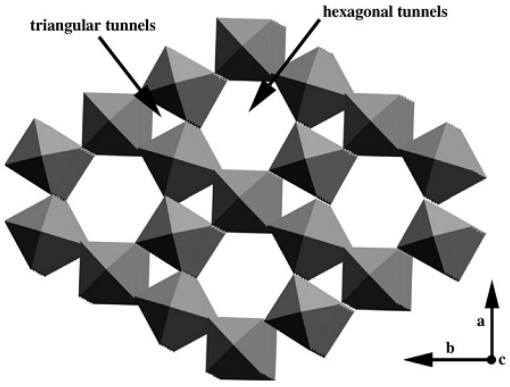

Figure 2.3 Arrangement of [W-O6] octahedral in the structure of hexagonal WO_3(Gu et al., 2007)

WO_3 has been examined as an anode material for lithium ion batteries due to enhanced safety because of high melting temperature and mechanical stability, low cost and large theoretical capacity (~700 mAh g−1) (Yoon et al., 2011). More importantly, a very high volumetric capacity can be expected considering its high theoretical density of 7.61 g/cm^3 (Yoon et al., 2011).

Like transition metal oxides (Mn_xO_y, NiO, Fe_xO_y, CuO, MoO_2, etc), the anode charging–discharging mechanism of WO_3 is based on conversion reaction, which requires formation of a metal and lithium oxide (Poizot et al., 2000). When WO_3 was applied as an anode material for lithium ion battery, a d ischarge

capacity of 200–600 mAh/g was obtained according to the following conversion reaction mechanism:

$$WO_3 + 6Li^+ + 6e^- \rightarrow W + 3Li_2O \quad \ldots\ldots (2.1)$$

$$W + 3Li_2O \rightarrow WO_3 + 6Li^+ + 6e^- \quad \ldots\ldots. (2.2)$$

Based on this reaction, the calculated theoretical capacity of WO_3 is 693 mAh/g, and a very high volumetric capacity can be expected considering its high theoretical density of WO_3(Gu et al., 2007). Furthermore, a WO_3 anode material is expected to be profitable in improving the safety of an LIB because of the strong mechanical stability and its intrinsic high melting temperature (Lide, 2004).

Nevertheless, WO_3 as an anode material has disadvantage, due to suffers from large structural and volume variation during the charge/discharge processes, and the induced structure change breaks the stability of electrode material, leading to mechanical disintegration and the loss of electrical connection between the active material and current collector. It can decrease the cycling ability and rate capability of electrodes. Moreover, after only several tens of cycles even at low current rates the capacities faded rapidly to lower than 75% of the initial values (Yu et al., 2013). Therefore, it is desirable to find suitable WO_3 properties which could improve its performance as anode material for lithium ion battery.

Gu et al., 2007 have prepared single-crystal nanowires of hexagonal tungsten trioxide in a large scale by a simple hydrothermal method without any templates and catalysts. However the electrode only delivered a low discharge capacity of 218 mAh/ with coulombic efficiency of 75.6% for the first cycle. Meanwhile An ordered mesoporous WO_{3-x} with high electrical conductivity (m-WO_{3-x}) was prepared and evaluated by Yoon et al., 2011 as an anode material for lithium ion batteries (LIBs). It exhibited a reversible capacity of 748 mAh/g and the coulombic efficiency of 53% at 1st cycle.

Yin et al., 2012 had synthesized γ-WO_3 hierarchical nanostructures by using a biomolecule-assisted hydrothermal approach between $Na_2WO_4 \cdot 2H_2O$ and glycine acid. This electrode has discharge capacity of 515.1 mAh/g and coulombic efficiency of 62.4% for the first cycle.

Nanostructured WO_3 thin film has been successfully fabricated by radio-frequency magnetron sputtering method. The reversible discharge capacity of

WO_3/Li cells cycled between 0.01 V and 4.0 V was found above 626 mAh/g during the first 60 cycles at the current density 0.02 mA/cm_2 (Li and Fu, 2010). However, this electrode has a high cost of the deposition process and low active material loading.

WO_3 hollow nanosphere is reported by Sasidharan et al., 2012 using polymeric micelle with core shell corona architecture. The nanostructured electrode delivers high initial discharge capacity of 1054 mAh/g at a charge/discharge 0.2 C. unfortunately, the capacity retention is only 28.4% after 50 cycles.

2.2 Graphene, Graphene Oxide and reduced Graphene Oxide

Graphene is a two dimensional of carbon, consisting of sp^2 hybridized carbon atoms arranged in a honeycomb crystal lattice which has a highly unique electronic structure because of the charge carriers behaving like relativistic particles(Novoselov et al., 2004). Graphene forms a basic structure of other carbon materials like graphite, fullerenes and carbon nanotubes. The ballistic charge transport at room temperature and at high charge carrier concentrations make graphene interesting for applications such as energy strorage device where electronic conductivity is of high importance(Geim and Novoselov, 2007).

Graphene can be prepared in various ways: reduction of graphene oxide (GO) (Li et al., 2008), epitaxial growth (Berger et al., 2006), micromechanical exfoliation of highly oriented pyrolytic graphite (Novoselov et al., 2004) and chemical vapor deposition (CVD) (Wintterlin and Bocquet, 2009). From the aforementioned methods, the reduction of GO is the most suitable for large-scale graphene production. It must also be noted that the vast majority of graphene composite lithium ion battery cathode materials use g raphene obtained by reducing GO(Kucinskis et al., 2013).

Currently one of the most popular to produce graphite oxide is the method first reported by Hummers and Offerman (Hummers and Offeman, 1958). Oxidized graphite has been prepared by treating graphite with a mixture of three oxidizing agents: sulfuric acid (H_2SO_4), sodium nitrate ($NaNO_3$) and potassium permanganate ($KMnO_4$). It is then rinsed with water and hydrogen peroxide and

filtered afterward. After that resinous anion and cation exchangers are used to remove the remaining impurities.

Although graphite oxide retains the stacked layer structure of graphite, it incorporates oxygen and hydrogen containing groups. These groups increase the interlayer distance and due to weakening of the platelete-platelete interactions make the atom-thick graphite oxide layers hydrophilic (Pei and Cheng, 2012). One or few monolayers of graphite oxide are called graphene oxide (GO). Sonicating and/or stirring GO in water are the most common method to exfoliate graphite oxide to graphene oxide (Dreyer et al., 2010).

D.C. Marcano et al. have been proposed improvement of the original Hummers method (Marcano et al., 2010). They found that excluding $NaNO_3$, increasing the amount of $KMnO_4$ and performing the reaction in a mixture of H_2SO_4/H_3PO_4 (9:1) improves the efficiency of the graphite oxidation process. Some less altered modifications of Hummers method have also been used; in most of these the main difference lies in the graphene to oxidants mass ratio used or oxidation times(Ding et al., 2010).

The precise chemical structure of both graphene and graphene oxide is yet to be fully understood due to its complexity and partial amorphous characteristics (Dreyer et al., 2010). However, the model was widely accepted is the one proposed by Lerf and Klinowski (Figure 2.4**)**.

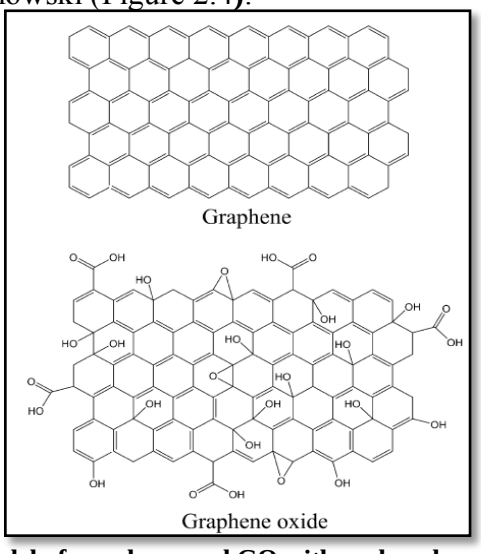

Figure 2.4 The structural model of graphene and GO with carboxyl groups at the sides(Lerf et al., 1998)

Graphene has a high ionic and electronic conductivity. In other hand, both graphite oxide and graphene oxide (GO) are electrically insulating materials due to their disrupted sp^2 bonding networks(Becerril et al., 2008). Functionalization present in GO breaks the conjugated structure and localizes p-electrons, resulting in a decrease of both carrier mobility and carrier concentration (Lerf et al., 1998). Reduction of GO results in a partial restoration of the electrical conductivity by restoring the p-network. The material obtained by reducing GO is generally referred to as reduced graphene oxide (rGO) or simply graphene(Kucinskis et al., 2013).

GO can be reduced chemically, thermally, electrochemically or by using combinations of several aforementioned methods. The most common method is chemically (Dreyer et al., 2010). In chemical reduction, the oxide functionality from the surface is stripped by using reducing compounds such as hydrazine and its derivatives (hydrazine monohydrate, dimethylhydrazine), $NaBH_4$ (Shin et al., 2009), ascorbic acid (Vitamin C) (Fernandez-Merino et al., 2010) hydroiodic acid (Pei and Cheng, 2012) and oxalic acid(Song et al., 2012).

Thermal treatment has been used for graphite oxide exfoliation and GO reduction and can be carried out in vacuum, inert or reducing atmospheres. When graphite oxide is subjected to high temperature heating, the oxygen-containing functional groups attached to the carbon plane are decomposed into gas phase (mostly CO_2) that create huge pressure between the stacked layers(Schniepp et al., 2006).

The thermal treatment can not only exfoliate graphite oxide, but also strip away some oxide functionalities from the surface of GO(McAllister et al., 2007), efficiently meaning that graphene can be obtained directly by thermal exfoliation of graphite oxide. Aside from the reduction of GO, thermal treatment is also found to remove chemical contaminants that can adhere to the graphene during processing and degrade its electronic properties(Schultz et al., 2011).

There are some research about graphene based anode material for lithium-ion batteries. A facile hydrothermal method was employed to prepare Fe_2O_3/graphene composites with different contents of graphene by Xiao et al., 2013. After performed as anode for lithium ion battery, Fe_2O_3/graphene

composite with graphene mass content of 30% exhibits outstanding cyclability with highly reversible charge capacity of 1069 mAh /g after 50 cycles, at current density of 50 mA/g. And when the current density is increased to 1000 mA/g, it could still retain charge capacity of 534 mAh/g.

Chen et al., 2012 used a facile ultrasonic method to synthesize CoO/graphene nanohybrids by employing $Co_4(CO)_{12}$ as a cobalt precursor. The CoO/graphene nanohybrids display high performance as an anode material for lithium-ion battery, such as high reversible lithium storage capacity (650 mA·h/g after 50 cycles, almost twice that of commercial graphite anode), high coulombic efficiency (over 95%) and excellent cycling stability.

TiO_2–graphene nanosheets (GNS) composites are prepared via an in situ chemical synthesis method, which enables a homogenous dispersion of TiO_2 nanoparticles on the graphene nanosheets. The TiO_2–GNS composites can deliver 60 mAh/g at a current rate as high as 5000 mA/g and demonstrate negligible fade even after 400 cycles. The superior electrochemical performances of the TiO_2–GNS composites can be attributed to their unique structures, which intimately combine the conductive graphene nanosheets network with uniformly dispersed TiO_2 nanoparticles(Tao et al., 2012).

MoO_2–graphene composite was synthesized via a t wo-step of hydrothermal-calcination method. When used as anode material for lithium ion batteries, the MoO_2–graphene composite shows an enhanced cyclic performance and lithium storage property. The first discharge capacity of the composite can reach 674.4 mAh/g with a reversible capacity of 429.9 mAh/g. Significantly, the composite can also deliver a reversible capacity of as high as 1009.9 mAh/g after 60 charge/discharge cycles(Yang et al., 2013b).

A new facile approach was proposed to synthesize nitrogen-doped graphene sheets with the nitrogen doping level as high as 7.04 weight % by thermal annealing pristine graphene sheets and low-cost industrial material melamine. The high-level nitrogen-doped graphene sheets exhibit a superhigh initial reversible capacity of 1123 mAh/g at a current density of 50 mA/g. More significantly, even at an extremely high current density of 20000 mA/g, highly stable capacity of about 241 mAh/g could still be obtained (Cai et al., 2013).

Three types of graphene papers, with thickness of 1.5, 3 a nd 10μm, respectively, were fabricated by vacuum-assisted filtration of reduced graphene nanosheets suspended in water. These papers deliver evidently different lithium storage capacities, with thinner papers always outperform thicker ones. The 1.5μm paper gives rise to initial reversible specific capacities (the first 10 cycles) of 200 mAh/g at a cu rrent density of ~100 mA/g, while the 10μm paper only presents ~80 mAh/g at a current density of 50 mA/g. After 100 cycles, a specific capacity of ~180 mAh/g is retained for the 1.5μm paper; in contrast, only ~65 mAh/g remains for the 10μm paper(Hu et al., 2013).

A simple urea-assisted, auto-combustion synthesis was used to fabricate pure Co_3O_4 nanoparticles and their nanocomposite with 10 w t% reduced graphene nanosheets. Using the Co_3O_4/CoO/graphene nanocomposite as an anode in lithium ion battery led to a higher lithium storage capacity than using pure Co_3O_4 nanoparticles electrode. The Co_3O_4/CoO/graphene nanocomposite electrode delivers an initial charge capacity of 890.44 mAh g−1 and exhibits 90% of good capacity retention (801.31 $mAh.g^{-1}$) after 30 cycles. While pure Co_3O_4 nanoparticles electrode (877.98 mAh g^{-1}) fades quickly, retains only 60% (523.94 mAh g−1) after 30 cycles (Rai et al., 2013a).

A ternary nanocomposite based on tin indium oxide (SnO_2–In_2O_3) and graphene nanosheet (GNS) was synthesized via a facile solvothermal method as an anode for lithium ion batteries. The SnO_2–In_2O_3/GNS nanocomposite exhibits a remarkably improved electrochemical performance in terms of lithium storage capacity (962 mAh/g at 60 mA/g rate), initial coulombic efficiency (57.2%), cycling stability (60.8% capacity retention after 50 cycles), and rate capability (393.25 mAh/g at 600 mA/g rate after 25 cycles) compared to SnO_2/GNS and pure SnO_2–In_2O_3 electrode(Yang et al., 2013a).

2.3 Hydrothermal Method

The controllable synthesis of highly ordered nanostructure has been widely studied by using kinds of methods, such as low temperature solution based chemical strategies including electrochemical synthesis method, hydrothermal method and the sol gel method (Liu et al., 2009); and high-temperature vapor-phase approaches including chemical vapor deposition and physical vapor deposition(Saron and Hashim, 2013). Among them, hydrothermal synthetic strategies on a water system are considered as simple and powerful routes and become more popular in fabricating ordered nanoarray structures(Yang et al., 2013b).

The main advantages that hydothermal method offers are: (1) simple and economical, (2) limited equipment corrosion problems, (3) operation the process does not require the addition and recovery of chemicals different from water and (4) the processing can be considered an environmentally friendly fractionation process(Romaní et al., 2010).

Hydrothermal technologies are broadly defined as chemical and physical transformations in high-temperature, high-pressure liquid or supercritical water (SCW) (Peterson et al., 2008). Hydrothermal degradation is an effective technology to decompose polymer derived from plants (Bobleter, 1994) and it is environment-friendly technologies that can be conceived as a first step for the chemical utilization of lignocellulose (Garrote et al., 1999).

As a low temperature technology, hydrothermal synthesis is environmentally friendly in that the reaction takes place in aqueous solutions within a closed system and using water as the reaction medium (Sayılkan et al., 2006). This technique is usually carried out in an autoclave (a steel pressure vessel) under controlled temperature and/or pressure. The operating temperature is held above the water boiling point to self-generate saturated vapor pressure (Chen and Mao, 2007). The internal pressure generated in the autoclave is governed by the operating temperature and the presence of aqueous solutions in the autoclave.

The hydrothermal method is widely applied in metal oxide production because of its many advantages, such as low energy requirement, simple control of the aqueous solution, high reactivity and relatively non-polluting set-up (Lee et

al., 2007). The reaction pathway is very sensitive to the experimental conditions, such as pH, temperature and hydrothermal treatment time.

1D or 2D nanoarrays like NiO nanorod, $Ni(OH)_2$ nanowall and Co_3O_4 nanowire/nanosheet arrays can be achieved via simple hydrothermal method of directly putting the substrates into corresponding reaction solutions, maintaining for a certain time at appropriate temperature and following annealing treatment (Figure 2.5). The morphology and size of these nanoarrays mainly depend on the reaction conditions, such as concentration and ratios of the reactants, reaction time and reaction temperature (Yang et al., 2013b).

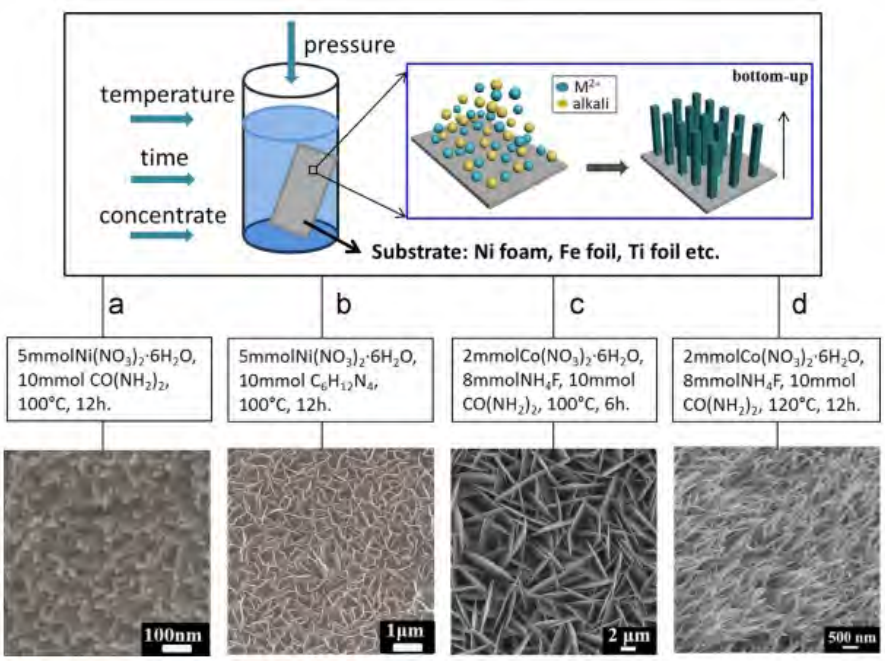

Figure 2.5 Schematic diagram of hydrothermal synthesis of 1D and 2D nanoarrays. (a) NiO nanorod; (b) $Ni(OH)_2$ nanowall; (c) Co_3O_4 nanosheet and (d) Co_3O_4 nanowire(Yang et al., 2013b)

Tungsten trioxide was synthesized using hydrothermal method. The chemical reactions that occurred in the preparing process are as follows (Zheng et al., 2013):

$$Na_2WO_4 + 2HCl + nH_2O \rightarrow H_2WO_4{\cdot}nH_2O + 2NaCl \quad (2.3)$$

$$H_2WO_4{\cdot}nH_2O \rightarrow WO_3 + (n+1)2H_2O \text{ (hydothermal process)} \quad (2.4)$$

At a relatively low pH value (pH of 1.5-2), a great deal of small WO_3 nuclei is quickly generated because heterogeneous nucleation onto a foreign surface

occurs readily compared to homogeneous nucleation in solution. The nuclei randomly distribute and scatter in all directions. Small WO_3 nuclei spontaneously aggregate into large spheres owing to the high concentration of H^+. The numbers of nuclei which make up large particles are different. And for each particles, the sizes of nuclei vary on a large scale. The nucleus begins to grow only when its size is larger than the critical size. When a large number of nuclei are generated, the supersaturation of H_2WO_4 reaches a low level, which creates the conditions for WO_3 growth(Zheng et al., 2013).

2.3.1 NaCl assisted Hydrothermal

Sodium chloride is an ionic compound with the formula NaCl, representing equal proportions of sodium and chlorine. Large quantities of sodium chloride are used in many industrial processes, and it is a major source of sodium and chlorine compounds used as feedstocks for further chemical synthesis(Kostick, 2014).

In solid sodium chloride, each ion is surrounded by six ions of the opposite charge as expected on electrostatic grounds. The surrounding ions are located at the vertices of a regular octahedron. In the language of close-packing, the larger chloride ions are arranged in a cubic array whereas the smaller sodium ions fill all the cubic gaps between them. This same basic structure is found in many other compounds and is commonly known as the halite or rock-salt crystal structure(Kostick, 2014). The properties of common NaCl are shown in the Table 2.2(John M. Hills, 2014):

Sodium chloride is readily soluble in water and insoluble or only slightly soluble in most other liquids. It forms small, transparent, colorless to white cubic crystals. Sodium chloride is odorless but has a characteristic taste. It is an ionic compound, being made up of equal numbers of positively charged sodium and negatively charged chloride ions. When it is melted or dissolved in water the ions can move about freely, so that dissolved or molten sodium chloride is a conductor of electricity; it can be decomposed into sodium and chlorine by passing an electrical current through it(Infoplease, 2014).

Table 2.2 The properties of NaCl(John M. Hills, 2014)

Name of compound	sodium chloride
Chemical formula	NaCl
Formula weight	58.443
Colour	colourless or white when pure; coloured splotches (*e.g.*, blue, purple) when impure
Lustre	vitreous
Physical form	transparent to translucent cubic crystals; also powder or granules
Mohs hardness	2 1/2
Density at 0° C (32° F)	2.17 g/cm³
Melting point	801° C (1,474° F)
Boiling point	1,465° C (2,669° F)
Solubility	water (s)*; glycerol (s); alcohol (ss)†; hydrochloric acid (i)‡
* (s) = soluble; † (ss) = slightly soluble; ‡ (i) = insoluble	

The chloride ions are also strongly solvated, each being surrounded by an average of 6 molecules of water. Solutions of sodium chloride have very different properties from pure water. The freezing point is −21.12°C (−6.02°F) for 23.31 wt% of salt, and the boiling point of saturated salt solution is near 108.7°C (227.7°F)(Ullmann and Elvers, 1991).

NaCl was used by Lu et al. (Liu and Aydil, 2009) for the growth of oriented single-crystalline rutile TiO_2 nanorods for dye-sensitized solar cells. When growth was conducted by adding saturated aqueous NaCl solution to the growth solution, the diameter, density, and alignment of the nanorods could be changed. The nanorods appear less aligned with the substrate surface normal because reduction of diameter and density decrease the probabilities of nanorods growing. The exact role of NaCl in controlling the diameter and density of the nanorod growth is not fully understood, but several explanations are possible. First, addition of sodium chloride salt greatly increases the ionic strength of the growth solution, and higher ionic strength favors the formation of smaller crystals through electrostatic screening(Vayssieres et al., 1998). Second, a layer of ions next to the nanorods can act as a diffusion barrier for the nanorod growth and

retard the precursors from diffusing to the surface(Xu and Zeng, 2003). Finally, Cl^- could preferentially adsorb and retard the growth rate of (110) surfaces.

The ability to retard the diameter growth rate through NaCl addition helps grow longer TiO_2 nanorods while avoiding the side surfaces from coalescing to form a continuous film. In control experiments, when no NaCl is added to the solution in the second step of the growth, the nanorods grow taller and wider, ultimately touching each other to form a continuous film with large grains at the bottom(Liu and Aydil, 2009).

Mesoporous Zr-incorporated MCM-41 can be synthesized in the acid conditions self-generated by the hydrolysis of $ZrOCl_2$ with the addition of NaCl. In this method, both NaCl and $ZrOCl_2$ are necessary for the self-assembly of surfactant micelle and inorganic species to ordered mesoporous materials(Yang et al., 2010). The ordering of Zr-MCM-41 could be greatly improved by the addition of NaCl in the synthesis gel. The optimal molar ratio of NaCl/Si was 1.0. The ordering decreased when the ratio was greater or smaller than this value. It revealed that NaCl played an important role in the self-assembly process of surfactant micelle and inorganic species. With the addition of NaCl, the large amount of Cl^- strengthened the electrostatic interaction between the surfactant micelle and inorganic species, and thus facilitated the formation of ordered mesostructure. However, too much NaCl seemed to hinder the self-assembly of the micelle and the inorganic precursors(Yang et al., 2010).

NaCl was also used for synthesis of radially aligned single-walled carbon nanotubes on a SiO_2/Si substrate(Rao et al., 2009). They showed that by using ferritin in NaCl solution as catalyst precursor, cristobalite could be identified on the SiO_2/Si substrate after the growth of SWCNTs. The addition of NaCl concentration in the solution could increases the signal intensity of cristobalite. The cristobalite peak is not observed if only a ferritin aqueous solution was used. Cristobalite is believed to be formed from the crystallization of amorphous SiO_2.

Lee et al. (Lee et al., 2009) had synthesized gold icosahedra and nanoplates using Pluronic P123 block copolymer and NaCl. They observed that the shape of the gold crystals could be changed from icosahedra to plates by introducing NaCl. NaCl promoted the growth perpendicular to the [111] direction

required for producing gold nanoplates. The concentration of NaCl could control the ratio of gold icosahedra to nanoplates. As the molar ratio of NaCl to the gold salt increases from 0 to 10, the size and shape of the gold icosahedra become smaller and more irregular, respectively, and their content in the product decreases, while that of the gold nanoplates increases(Lee et al., 2009).

2.3.2 Na-EDTA assisted Hydrothermal

Ethylenediamine tetraacetic acid (EDTA) and its salts are substituted diamines. These ingredients function as chelating agents by combining with polyvalent metal cations in solution to form soluble ring structures. EDTA and its salts have uses in pharmaceutical products, foods, and manufacturing and treat heavy metal poisoning(Lanigan et al., 2002).

EDTA is a white, odorless, nonhygroscopic crystalline powder. It decomposes over a melting range of 234 to 250^{o}C. The molecular weight of this compound is 292.24 gr/mol. EDTA is slightly soluble in water and solutions of alkali hydroxides, but it is insoluble in common organic solvents (Longer et al., 1990).

EDTA and its salts are chelating agents. They are neutralized by alkali-metal hydroxides to form water-soluble salts, or chelates, that contain metal cations(Budavari et al., 1989). Chelating agents such as EDTA are anionic. EDTA forms a t etranegative anion, and is strongly attracted to alkaline earth and transition metal ions. The metal ion is converted to an anionic form as part of a metal-EDTA complex during a reaction with EDTA; thus, the oxidation-reduction potential of the metal ion is altered and the partitioning of the metal to the aqueous phase is enhanced. The chelating action of EDTA occurs at alkaline pH as long as metallic ions are available, until all the EDTA molecules are utilized. One mole of EDTA chelates one mole of metallic ions(Saquy et al., 1994).

Generally, EDTA is stable as a solid and in aqueous solution. Only strong oxidizing agents can attack it chemically. The stability of EDTA-metal chelates increases according to the order(Heindorff et al., 1983) :

$$Na^{+} < Ca^{2+} < Fe^{2+} < Co^{2+} < Zn^{2+} < Cu^{2+} < Pb^{2+} < Fe^{3+}$$

Disodium EDTA is a w ater-soluble, almost odorless, white crystal or crystalline powder with a molecular weight of 336.21 to 372.24 gr/mol. Disodium EDTA decomposes at 252^{o}C. The melting point of disodium EDTA is 240^{o}C, the ash point is >100^{o}C, and it is soluble in water (~100 g/l) at 20^{o}C (Longer et al., 1990).

Disodium EDTA has some characteristics of weak acids; it displaces carbon dioxide from carbonates and reacts with metals to form hydrogen(Budavari et al., 1989). Disodium EDTA was prepared by dissolving EDTA into a hot solution that contained two equivalents of sodium hydroxide. The solution then was allowed to crystallize(Longer et al., 1990).

EDTA and its salts have been effectively employed in the hydrothermal process as a structure-directing agent and chelating ligand to produce nano crystals with different morphologies (Ha et al., 2009). Among the complexing agents, EDTA and Na_2-EDTA are known to be particularly efficient due to the presence of amine groups in these molecules. Such molecules can effectively complex metal ions of different sizes, and help in achieving chemical homogeneity in the end products. However the high chelating abilities of EDTA and Na_2-EDTA has not been widely used as a fuel in solution combustion reactions(Hari Krishna et al., 2014).

Krishna et al. (Hari Krishna et al., 2014) used EDTA and Na_2EDTA for synthesis of Y_2O_3 as photo- and thermo-luminescent applications. They show that lowest crystallite size is observed for sample prepared using EDTA fuel due to amorphous nature of the product. Whereas, crystallinity and crystallite size increases for sample prepared using Na_2EDTA.

Wang et al. (Wang et al., 2009) used Na_2EDTA mediated hydrothermal to synthesis of YVO4:Eu^{3+}. They show that the addition of additive agents can affect the nucleation and growth of particles, which consequently can modify particle morphology and size. The different pH value can induce different modality of Na_2EDTA. When the pH value of synthesis solution ranged from 1 to 4, the $EDTA^{2-}$ ions are few, the process of formation YVO4:Eu^{3+} structures are mainly the homogeneous precipitation process. When the pH value was increased to 7 and 14, the Na_2EDTA leads to the anisotropic growth of nano-particles. Because

it is clear that a strong ligand (Na_2EDTA) is not only needed to form a stable complex with Y^{3+}, but also the ligand binds to the surface of the crystal, which directly affects the growth direction and crystal structure of the nano-crystals(Wang et al., 2009).

$LaPO_4$ had been synthesized by Dong et al. (Dong et al., 2010) using EDTA assisted hydrothermal method. They show that the as-prepared sample prepared with 1 mmol EDTA consist of rod-like particles with the size range of 500-1000 nm in width and about 1 mm in length. Moreover, the aspect ratio of the phosphors increases with the increase of EDTA concentration. Finally, the rod-like shape of the sample is changed to the wirelike morphology when the EDTA amount was increased from 1 mmol to 3 mmol(Dong et al., 2010).

Hariharan et al. (Hariharan et al., 2011) reported that the use of EDTA during the microwave hydrothermal synthesis of $W_{18}O_{49}$ nanoplate resulted oxygen vacancy. This is due to the fact that Na^+ ion of disodium salt of EDTA has a strong tendency to react with oxygen and forms intermediate Na_2O during the anneling process. This phenomenon decreases the concentration of oxygen in the WO_3 lattice and creates oxygen vacancy (Adhikari et al., 2014).

WO_3 hierarchical structure was synthesiszed by Rajesh et al. (Adhikari et al., 2014) using EDTA mediated microwave hydrothermal. The result revealed that the addition of EDTA leads to the controlled aggregation of WO_3 nanoparticles having high crystallinity with monoclinic structure and creates oxygen vacancy in the WO_3 lattice. Moreover, at high concentration of EDTA, cauliflower like hierarchical structure was formed when the optimum concentration of EDTA reaches to 0.5 mol (Adhikari et al., 2014).

EDTA has a significant effect on the size, morphology and aggregation of the product. EDTA also play an important to control the degree of crystalinnity (Ha et al., 2009). As the concentration of EDTA increases, the effect of chelation increases that controls the aggregation of WO_3 nanoparticles and forms the hierarchical structure(Adhikari et al., 2014). Furthermore, the surface area of WO_3 prepared in presence of EDTA is lesser than that of WO_3 preapared in absence of EDTA which is attributed to the formation of hieracrchical

structure(Adhikari et al., 2014). The schematic illustration for the formation of hierarchical WO_3 structure is show in Figure 2.6.

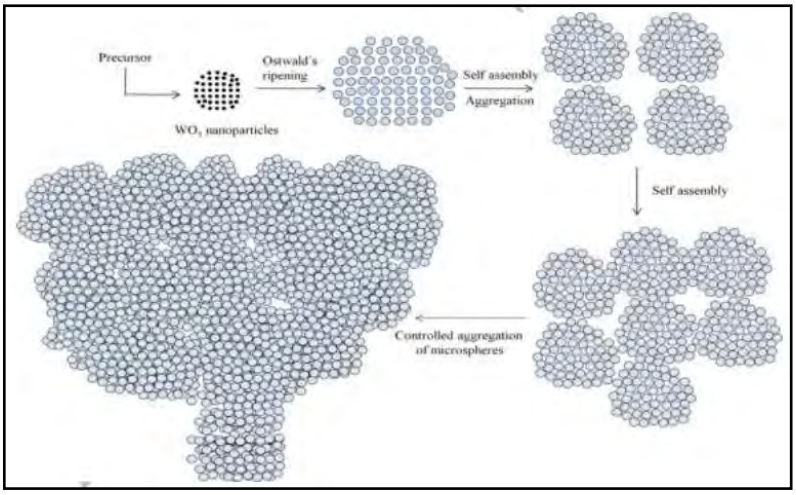

Figure 2.6 Schematic illustration of formation of hierarchical WO_3 structure in presence of disodium salt of EDTA under microwave hydrothermal condition(Adhikari et al., 2014)

(This page is empty deliberately)

CHAPTER 3
EXPERIMENTAL

3.1 Materials

Materials which be used in this work are:

a. $Na_2WO_4.2H_2O$
b. NaCl
c. Na EDTA
d. HCl
e. Distilled water
f. Graphite powder KS-4 (Timcal)
g. H_3PO_4 (>95%)
h. H_2SO_4 85%
i. $KMnO_4$
j. H_2O_2
k. PVDF
l. NMP
m. Carbon black (Super P)
n. Cu foil
o. Coin cell part

3.2 Instruments

Instrument which be used in this work are :

a. Analitic balance
b. Beaker Glass
c. Measuring tube
d. Dropper
e. spatula
f. stirrer
g. two neck bottle
h. ultrasonicator
i. Centrifuge machine and centrifuge tube

j. Autoclave
k. Oven
l. Glove box
m. Material characterization and electrochemical measurement:
    a) X-Ray Difraction (XRD) : Bruker D2 phaser
    b) Scanning Electron Microscope (SEM) : JEOL JSM 5800
    c) Thermal gravimetric Analysis : TA Instruments Q500 TGA
    d) Raman Measurement : Protrustech ProMaker Raman
    e) Cyclic Voltammetry (CV) : EC Lab V10.34
    f) Charge discharge : Acutech system Bat-750B (Ubiq machine)

3.3 Experiment Procedures

3.3.1 Synthesis of WO_3 via Hydrothermal Method

$Na_2WO_4.2H_2O$ was used as tungsten source, NaCl was used as crystal modifier to promote of the WO_3 nanoparticle, whereas Na-EDTA has been effectively employed in the hydrothermal process as chelating ligand and capping reagent to ptoduce one-dimensional nanostructure of WO_3.

WO_3 was synthesized by using different sodium salts. While other parameters were fixed, such as WO_4^{2-} concentration = 3 mmol/40 ml, HCl concentration = 5 mmol/40 ml, identical reaction temperature =180^oC and identical reaction time = 2 0h. The detailed process for synthesis was a follow(Figure 3.1). In a typical synthesis, 1 g $Na_2WO_4.2H_2O$ and a specified amount of NaCl and/or Na-EDTA were dissolved in 40 ml distilled water and kept stirring for 0.5 h. Hydrochloric acid solution was added dropwise to the above solution under stirring vigorously until the pH value of the solution was adjusted to approximate 1.5. The solution was then transferred into a stainless steel autoclave heated at 180^oC for 20 h , and then cooled down to room temperature naturally. The precipitate was centrifuged, washed with ethanol and deionized water several times and finally dried at 80^oC for further characterization. For comparison purposes, bare WO_3 was prepared through the

similar procedure above without adding either NaCl or Na-EDTA precursor in the process.

In the second section, WO_3 was synthesized with different temperature, but other parameters were fixed, such as WO_4^{2-} concentration = 3 mmol/40 ml, NaCl concentration= 3.3 mmol/40 ml, Na-EDTA= 3.3 mmol/40 ml, HCl concentration = 5 mmol/40 ml, and identical reaction time = 20 h. The temperatures were varied at 150°C, 180°C and 210°C. Subsequently, in the third section, WO_3 was synthesized with different amount of Na-EDTA, but other parameters were fixed, such as WO_4^{2-} concentration= 3 mmol/40 ml, NaCl concentration= 3.3 mmol/40 ml, HCl concentration= 5 mmol/40 ml, identical reaction temperature= 210°C and identical reaction time= 20 h.

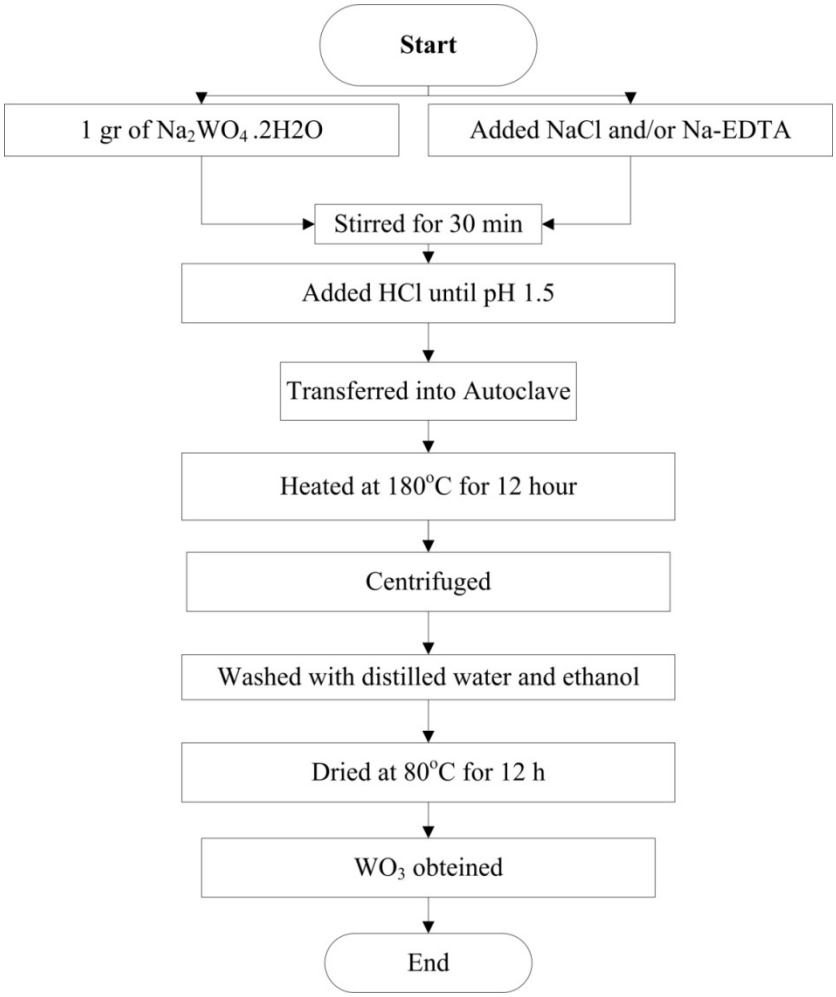

Figure 3.1 Flow chart of synthesis of WO_3 by using NaCl and/or Na-EDTA

3.3.2 Synthesis of WO_3/rGO composites

Graphene oxide was added into synthesis process of WO_3 to improve its cyclability and rate capability as anode material for lithium ion battery. This work was started by synthesis of graphite oxide (GO) and then mixed GO into WO_3 precursors via hydrothermal process to form WO_3/rGO nanocomposite.

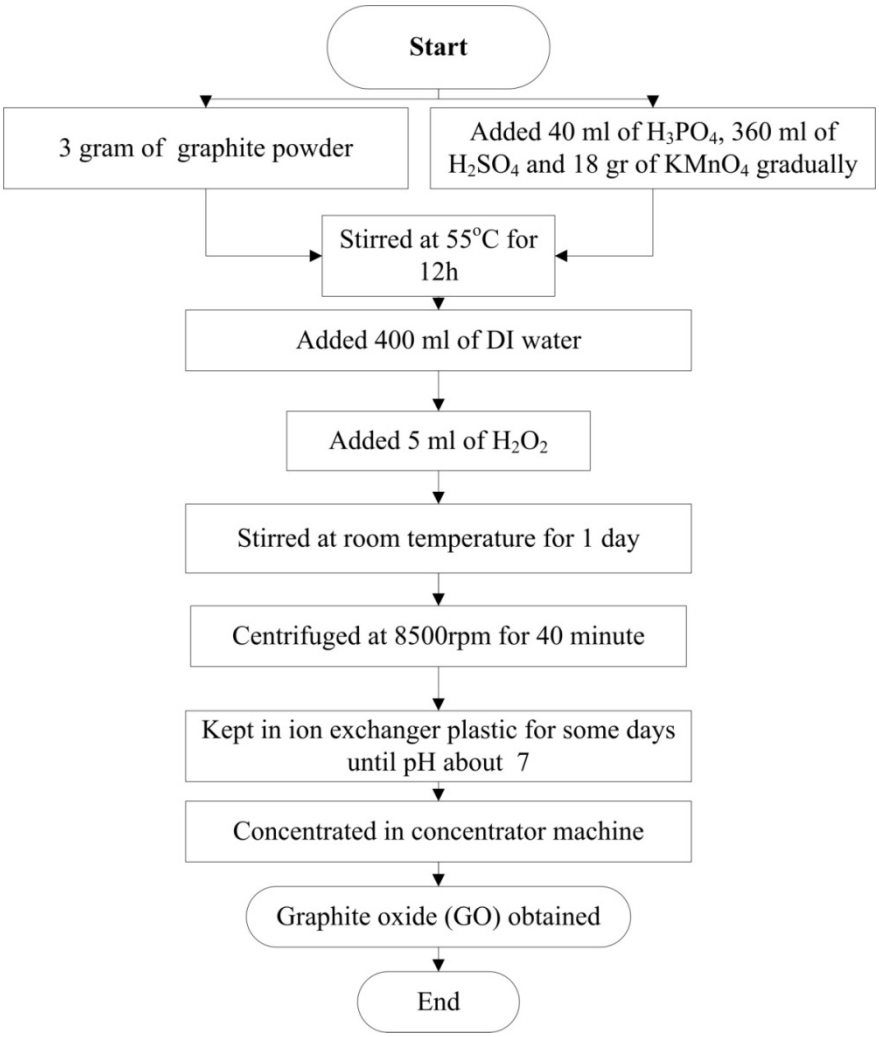

Figure 3.2 Flow chart of synthesis of graphite oxide

Graphite oxide is prepared from graphite powder KS-4 (Timcal) according to a modified Hummers method(Marcano et al., 2010). In a typical synthesis (Figure 3.2), 3.0 g of graphite powder was poured into two neck bottle which placed on ice bath cold (0◦C). Then, 40 ml of H_3PO_4, 360 ml of H_2SO_4 and 18 gr $KMnO_4$ were added gradually under stirring. Subsequently, the mixture was moved on oil bath and heated at 55°C for 12h under vigorous stirring. Then, the

mixture was diluted with 400 mL of deionized water. Because of the addition of water in concentrated sulfuric acid medium released a large amount of heat, the addition of water was performed in an ice bath to keep the temperature below 100^{o}C. The reaction was terminated by adding 5 mL of H_2O_2 solution and stirred for 1 day. The solid product was separated by centrifugation at 8500 rpm for 40 minute. For further purification, the resulting solid was kept in ion exchanger plastic which submerged in DI water until pH about 7. The suspension was concentrated by using concentrator machine to get x weight% graphite oxide (GO). Finally, GO suspension was dispersed in deionized water to create a homogeneous dispersion through ultrasonication for half an hour.

WO_3/rGO nanocomposite was synthesized through an in situ hydrothermal process. In a typical process (Figure 3.3), 1 g $Na_2WO_4.2H_2O$ and 0.2 g NaCl were dissolved in 40 ml GO solution and kept stirring for 0.5 h. Hydrochloric acid solution was added dropwise to the above solution under stirring vigorously until the pH value of the solution was adjusted to approximate 1.5. The solution was then transferred into a stainless steel autoclave heated at 180^{o}C for 20 h, and then cooled down to room temperature naturally. The precipitate was centrifuged, washed with ethanol and deionized water several times and finally dried at 80^{o}C for further characterization.

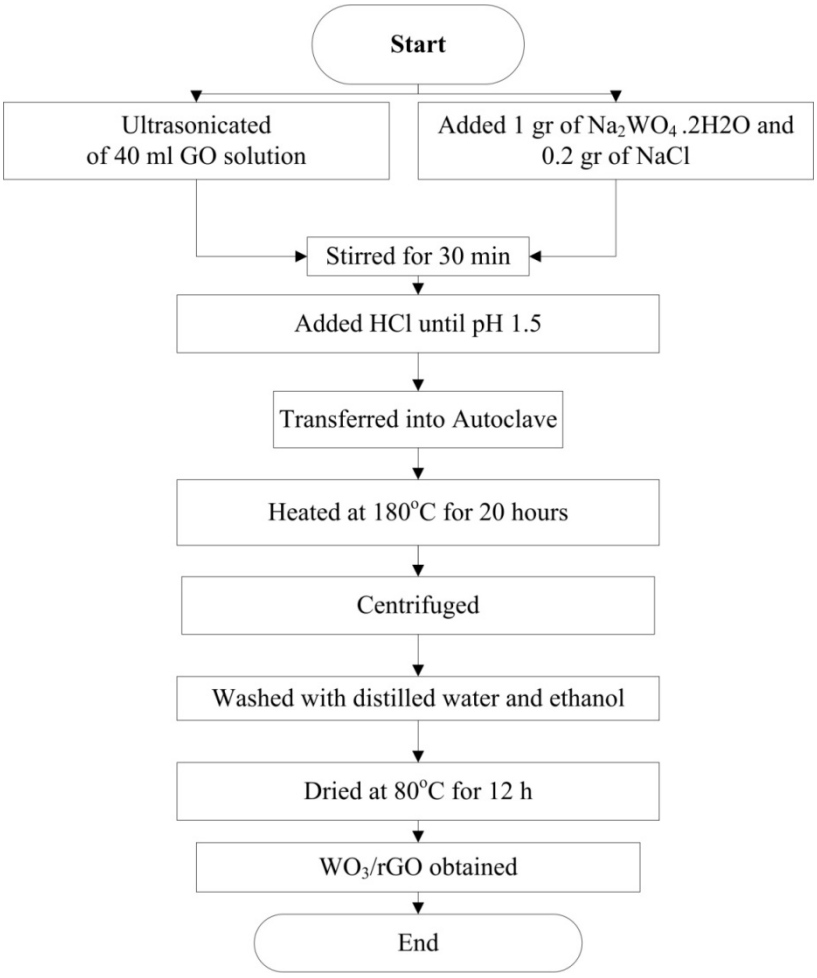

Figure 3.3 Flow chart of synthesis of WO_3/rGO

3.4 Material Characterization

Material characterizations of WO_3 were investigated using several common techniques such as X-Ray Diffraction (XRD), Field Emission Scanning electron Microscopy (FE-SEM), Thermal Gravimetric Analysis (TGA) and Raman spectroscopy.

3.4.1 X-ray Diffraction

The purity of synthesized samples were characterized by X-Ray Diffraction : Bruker D2 Phaser **(**Figure 3.4**)** . The Spectra from Cu Kα (λ= 15.406 Amstrong) λ= 1.5406 Å, Ni filter, 40 kV and 100 mA was recorded between the diffraction angle (2θ) from 20^o to 70^o. Low scanning rate was chosen with step size of 0.05^o and time of 0.5 second per step. The obtained XRD patterns were then compared with JCPDS reference from PCPDFWIN 2.1 software. For crytalline size calculation, Scherrer equation (eq. 3.1) was applied.

$$d = \frac{K.\lambda}{B.\cos\theta} \qquad \text{.....3.1}$$

where : d = crytalline size (Å)

K = shape factor (throughout this study K = 0.9)

λ = X-ray wavelength (Cu Kα = 1.5406 Å)

B = full width at half height maximum, FWHM

θ = angle (degree)

Figure 3.4 Bruker D2 Phaser XRD

3.4.2 Scanning Electron Microscopy

Scanning Electron Microscopy (FE-SEM) was used to visualize very small topographic details on the surface or entire or fractioned objects. SEM produces clearer, less electrostatically distorted images with spatial resolution down to 1.5 nm which it is 3 to 6 times. Smaller-area contamination spots can be examined at electron accelerating voltages compatible with Energy Dispersive X-ray Spectroscopy. Reduced penetration of low kinetic energy electrons probes closer to the immediate material surface. Moreover, SEM can obtain high quality, low voltage images with negligible electrical charging of samples.

The morphology of samples were investigated by SEM - JEOL JSM 5800 (Figure 3.5) using 15keV of energy with different magnification from 1k times to 10k times enlargement.

Figure 3.5 SEM- JEOL JSM-5800

3.4.3 Thermo gravimetric analysis

Thermogravimetric analysis (TGA) is commonly used to determine selected characteristics of materials that exhibit either mass loss or gain due to decomposition, oxidation, or loss of volatiles. TGA can provide information about physical phenomena, such as second-order phase transitions, including vaporization, sublimation, absorption, adsorption, and desorption. Likewise, TGA can provide information about chemical phenomena including chemisorptions, desolvation, decomposition, and solid-gas reactions

Samples were measured under air flow with a TA Instruments Q500 TGA (Figure 3.6) to know graphene content in samples. Sample sizes of 5-10 mg WO_3/graphene were loaded into platinum pans and heated from room temperature to 900^{o}C at air atmosphere with a heating rate of 10^{o}C/min.

Figure 3.6 TA Instruments Q500 TGA

3.4.4 Raman Spectroscopy

Raman spectroscopy uses a monochromatic laser to interact with molecular vibrational modes and phonons in a sample, shifting the laser energy down (Stokes) or up (anti-Stokes) through inelastic scattering. Identifying vibrational modes using only laser excitation, Raman spectroscopy has become a powerful, noninvasive method to characterize graphene and related materials.

To investigate the result of doping process of graphene, the Raman spectra of the samples were obtained by Protrustech ProMaker system (Figure 3.7) from Raman shift of 500 to 2000 cm^{-1}.

Figure 3.7 Protrustech ProMaker Raman

3.5 Electrochemical Measurement

3.5.1 Preparation of Electrochemical Measurement

For electrochemical measurement, a composite electrode was prepared as follows: a mixture of 70wt% active material, 10 wt% carbon black (Super P) and 20 wt% polyvinylidinedifluoride (PVDF) was dissolved in N-methylpyrrolidone (NMP), stirred vigorous for 1.5 h. Then the slurry was coated onto a Cu foil current collector with a blade. The electrode was dried for 12 h at 80◦C in a vacuum oven, followed by pressing compactly with a roller press machine. The CR2016 coin type cells (Figure 3.8) were assembled in an Argonfilled glove box (MBraun Lab Master 130, Germany). Lithium metal foil was used as the cathode and a polypropylene membrane was used as a separator. The electrolyte was composited of 1 M $LiPF_6$ in ethylene carbonate (EC) : dimethyl carbonate (DMC) (1:1, v/v).

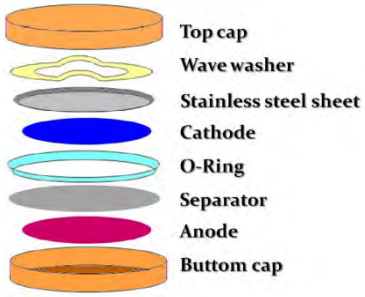

Figure 3.8 Schematic arrangement of coin cell assembly(Felix, 2012)

3.5.2 Galvanostatic charge-discharge

Galvanostatic charge-discharge of electrodes were measured by using Ubiq machine (Acutech System Bat-750B) between 0.01-3.0 V (vs Li/Li^+) with different current rate (C_{rate}) every 5 cycles from 0.1C, 0.2C, 0.5C, 1C, 2 C, 3C to 4 C (1C=693 mA/gr). And then to investigated the cycle life performance, the current density of 700mA/gr was applied on electrodes for 100 cycles.

3.5.3 Cyclic voltametry

Cyclic voltammetry tests were conducted by using an electrochemical workstation EC Lab V10.34 with range voltage 0.01-3.0 V (vs SCE) and scan rate 1 mV/s for 3 cycles.

(This page is empty deliberately)

CHAPTER 4
RESULTS AND DISCUSSION

4.1 WO_3 via hydrothermal method using different sodium salts

4.1.1 Material Characterization of WO_3 via a hydrothermal method using different sodium salts

The objective of this study is to obtain WO_3 nanostructure as anode material for lithium ion battery. WO_3 was synthesized via hydrothermal method using different sodium salts: NaCl and Na-EDTA. The as-synthesized WO_3 using NaCl only, WO_3 using Na-EDTA only and WO_3 using both of NaCl+Na-EDTA are labeled as WO_H180T20_C, WO_H180T20_E and WO_H180T20_CE, respectively. While the as-synthesized WO_3 without using either NaCl or Na-EDTA is labeled as WO_H180T20. Label of H180T20 represent that the products are synthesized at temperature of 180^{o}C for 20 hours.

Figure 4.1 shows the XRD patterns of the as-synthesized products at 180^{o}C for 20 h with different sodium salts. All the diffraction peaks can be indexed to hexagonal tungsten oxide (h-WO_3) with the space group P6/mmm (JCPDS 75-2187). No peaks of any other phases or impurities were observed from the XRD patterns, indicating that h-WO_3 crystalline phase with high purity could be obtained using the present synthetic process. However, the location of the strongest diffraction peaks is obviously different. In XRD pattern of WO_H180T20 and WO_H180T20_C, the intensity of diffraction peaks of (200) crystal plane is much higher than that of other peaks, suggesting that the WO_3 grows along [200] direction which it is due to NaCl effect. In other hand, when Na-EDTA are added, the intensity of the (001) diffraction peak greatly increases, suggesting that the WO_3 grows along [001] direction for WO_H180T20_E and WO_H180T20_CE. Subsequently, the crystalline size was estimated by Scherrer equation (eq.3.1) based on (001) and (200) plane and shown in

Table 4.1. It is seen that the crystalline size in (200) plane grows bigger when NaCl was added meanwhile the crystalline size in (001) plane grows bigger when Na-EDTA was added.

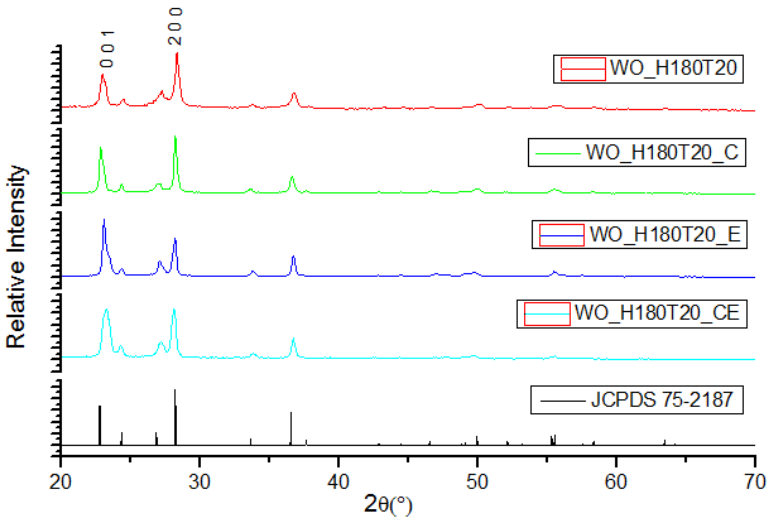

Figure 4.1 XRD pattern of WO_3 synthesized at 180°C for 20 h with different sodium salts: WO_H180T20 (without NaCl/Na-EDTA), WO_H180T20_C (NaCl only), WO_H180T20_E (Na-EDTA only) and WO_H180T20_CE (NaCl &Na-EDTA)

Table 4.1 The crytalline size of WO_3 synthesized at different sodium salts

Sample Label	Heat Treatment	D (nm)	
		(001) plane	(200) plane
WO_H180T20	180°C, 20 h	17.9	24.1
WO_H180T20_C	180°C, 20 h	21.6	34.5
WO_H180T20_E	180°C, 20 h	26.1	27.9
WO_H180T20_CE	180°C, 20 h	14.2	22.6

The morphology of the as-synthesized products observed using SEM, shown in Figure 4.2. It seen that the morphology of the as-synthesized WO_3 without using either NaCl or Na-EDTA is nanoparticle with huge agglomeration (Figure 4.2a). When NaCl was introduced into sample, the nanoparticle was still obtained but the aggregation was decreased (Figure 4.2b). From Fig. 4.2 (a) and (b), these are noted that the primary product of WO_H180T20 and WO_H180T20_C are nanoparticles, so the intensity of diffraction peak of (200) crystal plane is much higher than that of other peaks as shown in Figure 4.1.

With adding NaCl, the WO_3 nuclei grow along the direction which is vertical to the crystal surface with high surface energy. Furthermore, NaCl plays an important role in inducing the growth along [200] direction and in the mean time, reducing the growth along other directions. Then the larger nuclei grow into

nanoparticles along the [200] direction and act as “leader crystals” (Gu et al., 2005) for the growth of subsequent nanoparticles in parallel with the leader crystals.

When Na-EDTA are added, flake like structures are gained as shown in Figure 4.2 (c) which the intensity of the (001) diffraction peak in the XRD patterns greatly increases, suggesting that the WO_3 nanoflake grow along [001] direction. Furthermore, the nano crystal of WO_3 grows up with good aggregation and ultimately form the microflakes.

With adding of NaCl and Na-EDTA, the orientation of the WO_3 gets better (Figure 4.2d). Evidently, the presence of NaCl and Na-EDTA can affect the formation of well aligned WO_3, that is to say, the amount of NaCl and Na-EDTA added into the precursor solutions plays a key role in controlling the orientation of the synthesized WO_3. And it reveals that the WO_3 assumes the flake like structure composed of numerous microspheres which further composed of WO_3 nanoparticles. It can be seen that the NaCl and Na-EDTA have significant effect on the morphology, size and aggregation of the products (Adhikari et al., 2014).

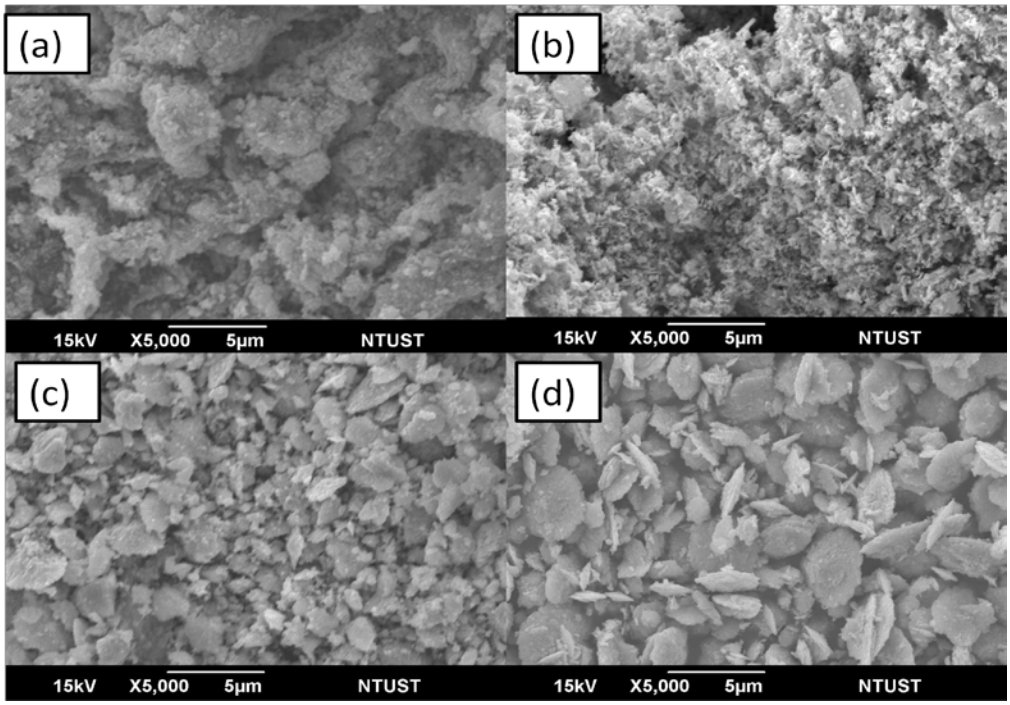

Figure 4.2 SEM Images of the synthesized WO_3 with diferrent sodium salts: (a) WO_H180T20, (b) WO_H180T20_C, (c) WO_H180T20_E and (d) WO_H180T20_CE

4.1.2 Electrochemical characterization of WO_3 via a hydrothermal method using different sodium salts

Figure 4.3 (a-d) show the galvanostatic charge/discharge pattern of WO_3 electrodes at a current rate of 0.1 C at 1st five cycles. Electrochemical reaction of WO_3 with lithium involve multi step for its decomposition and formation. The electrochemical performance evaluation is given in

Table 4.2. It can be seen that WO_H180T20_CE has the best performance towards 1st coulombic efficiency (85.3%) compared to others, and this can be attributed to its surface area and electronic conductivity. Meanwhile, WO_H180T20 and WO_H180T20_C have a low 1st coulombic efficiency that indicated large initial capacity loss. The large initial capacity loss of the samples can be partly attributed to the formatton of solid electrolyte interphase (SEI) layer on the electrode surface during the first discharging step, as well as the storage Li^+ in hollow WO_3, which are difficult to be extracted(Yin et al., 2012).

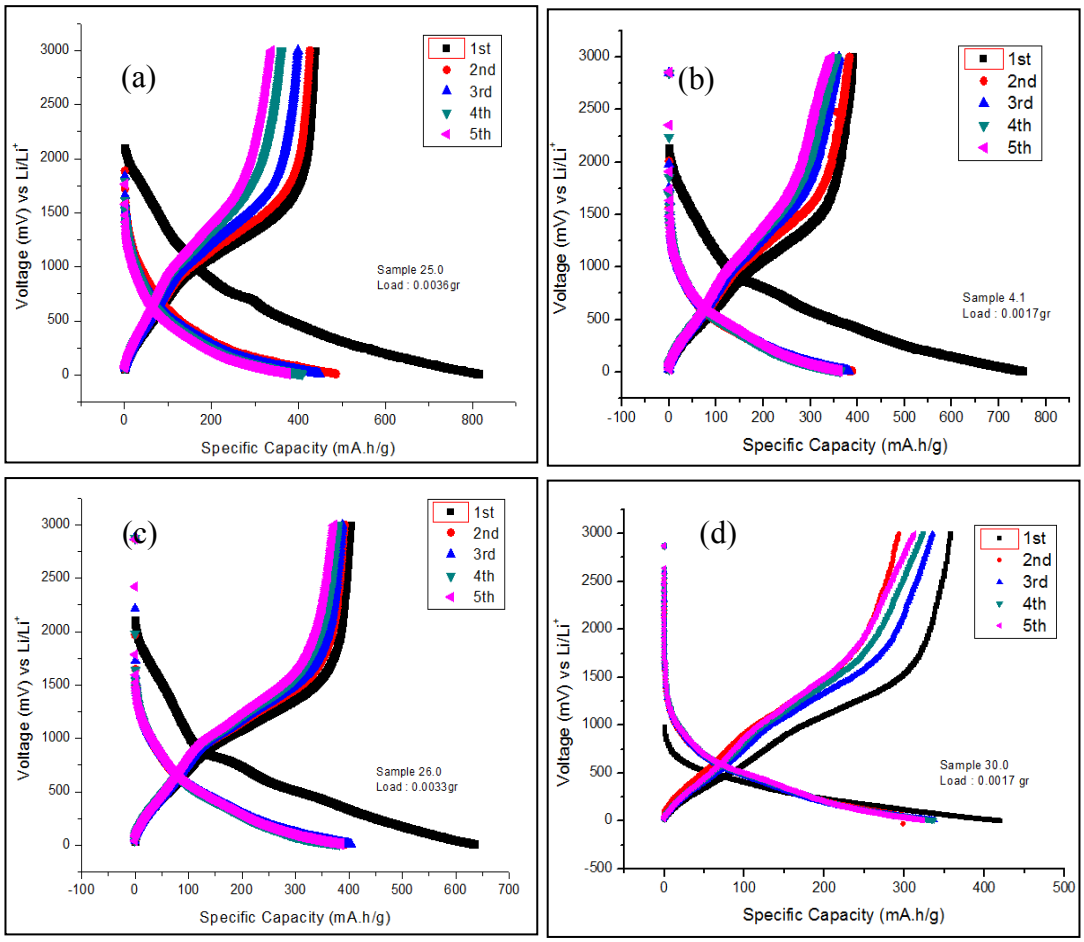

Figure 4.3 Charge/discharge curves of (a) WO_H180T20, (b) WO_H180T20_C, (c) WO_H180T20_E, (d) WO_H180T20_CE at 0.1C between 3.0V and 0.01V (vs. Li/Li+).

Table 4.2 First discharge capacity and coulombic efficiency of WO_3 with different Na salts

Sample code	Hydrothermal Treatment	1st discharge capacity (mAh/g)	1st coulombic efficiency (%)
WO_H180T20	180°C, 20h	814.27	53.73
WO_H180T20_C	180°C, 20h	750.40	51.85
WO_H180T20_E	180°C, 20h	635.06	63.47
WO_H180T20_CE	180°C, 20h	418.50	85.30

Figure 4.4 (a–b) shows the cyclic voltammograms of WO_H180T20 and WO_H180T20_C electrodes for the 1st three cycles. In the 1st cycle for WO_H180T20 and WO_H180T20_C, a reduction peak at ~0.98 V and oxidation peak at ~1.2 V are attributed to the lithium intercalation/ deintercalation according to the reaction: $WO_3 + xLi^+ + xe^- \rightarrow Li_xWO_3$. The reduction peak at ~0.5 V is ascribed to the formation of Li_2O resulting from the conversion reaction: $Li_xWO_3 + (6\text{-}x)Li \rightarrow W + 3Li_2O$(Yin et al., 2012) and accompanying decomposition of nonaqueous electrolyte. From 2nd cycle onwards the reduction peak at 0.5 V disappears while new reduction peak appear at ~1 V. This change can be accounted by the formation of a gel-like polymer layer formed out of the dissolution of the Li_2O in the electrolyte. Importantly, a pair peak at 1 V (cathodic sweep) and 1.2 V (anodic sweep) shows a good reversible capacity of electrodes after 2nd cycle. The cathodic and anodic peaks of the electrodes in general show a much more stable profile and tend to overlap each other. The CV curves are well consistent with the galvanostatic cycling profile.

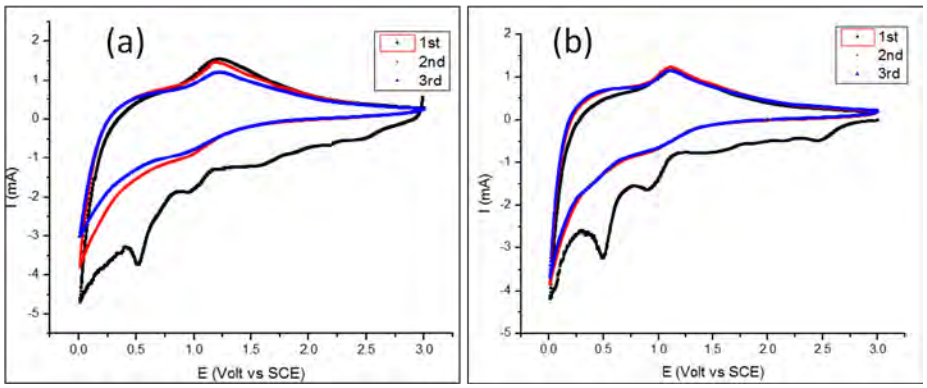

Figure 4.4 Cyclic voltammogram of (a) WO_H180T20 and (b) WO_H180T20_C for the 1st three cycles at scan rate 1 mV/s

Figure 4.5 (a) shows rate performance of WO_H180T20, WO_H180T20_C, WO_H180T20_E and WO_H180T20_CE at different current rate from 0.1C to 4C (1C = 693 mA/gr) between 3.0V and 0.01V (vs. Li/Li^+). The electrodes have been discharged and charged for 5 cycles at each current rate. At 0.1 C rate (corresponding to a time of 10 h to fully discharge the capacity), the WO_H180T20_CE electrode discharges to an averaged capacity of 410 mAh/g, while it reaches about 40 mAh/g at the highest rate tested (4 C), corresponding to a time of 900 s to fully discharge the capacity. Obviously, the capacity decreases stepwise when the rate increases. When the rate returns back to 0.1 C, the WO_H180T20_CE electrode discharges to 370 mAh/gr in averaged. This result indicates that the WO_H180T20_CE material presents the excellent structure stability. That means the capacity retention of WO_H180T20_CE is excellent due to the hierarchical structure of WO_3 which can storage more lithium. Whereas, WO_H180T20 shows drastic reduction in the capacity when the current rate increased to 0.5 C.

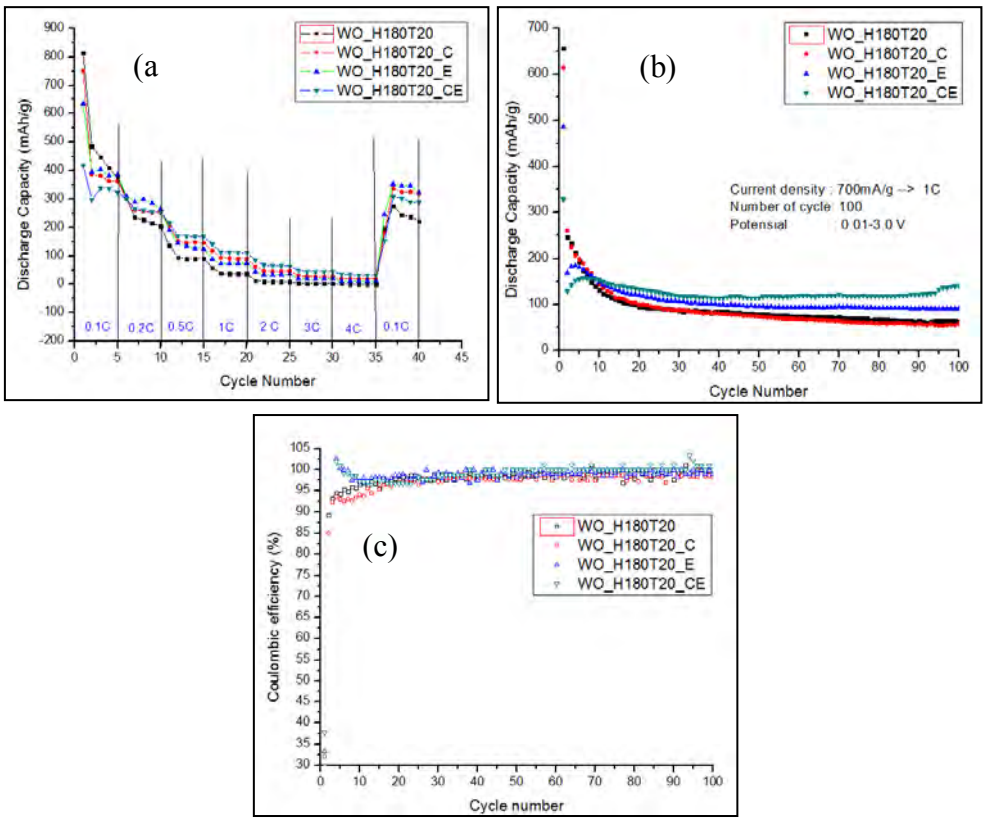

Figure 4.5 (a) Rate cycling performance with increasing current density of the synthesized WO_3 with diferrent sodium salts; (b) Cyclability and (c) coulombic efficiency at current density = 700 mA/g of WO_H180T20, WO_H180T20_C, WO_H180T20_E and WO_H180T20_CE

The cycling and stability testing of products were tested by measuring the cycle-life performance of electrodes up to 100 cycles at a current density of 700 mA/g (Figure 4.5 (b)). The specific capacity of WO_H180T20_CE material reaches 160 mAh/g for the tenth cycle while it remains 150 mAh/g for the 100th cycles. It show that WO_H180T20_CE also has a good stability and cyclability. In contrary, WO_H180T20 electrode shows extremely worse cycle performance which may be due to collapse of partial structure after 100 cycles. This result indicates that the WO_3 nanoparticles electrode (WO_H180T20) is unstable during electrochemical test compared to the WO_3 hierarchical structure electrode (WO_H180T20_CE). It can be concluded that WO_H180T20_CE has better electrochemical performance compared to WO_3 nanoparticles.

4.2 WO_3 via a NaCl & Na-EDTA-assisted hydrothermal with different reaction temperature

4.2.1 Material characterization of WO_3 via a NaCl & Na-EDTA-assisted hydrothermal with different reaction temperatures

The further investigation is to study the effect of reaction temperature on the morphologies and electrochemical properties of WO_3. For this section, the experiment was carried out in identical concentration (WO_4^{2-} concentration= 3 mmol/40 ml, NaCl concentration= 3.3 mmol/40 ml, Na-EDTA= 3.3 mmol/40 ml, HCl concentration = 5 mmol/40 ml) and the identical reaction time of 20 h, but with different reaction temperatures, those are 150, 180 and 210°C and the corresponding final products were labeled as WO_H150T20_CE, WO_H180T20_CE and WO_H210T20_CE, respectively.

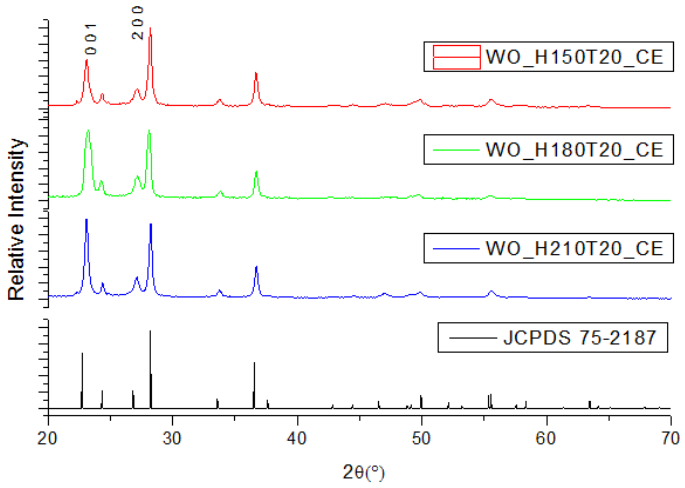

Figure 4.6 XRD pattern of WO_3 synthesized at different temperatures: WO_H150T20_CE (150°C), WO_H180T20_CE (180°C) and WO_H210T20_CE (210°C)

Figure 4.6 shows the XRD patterns of the WO_3 products at different temperatures. All the diffraction peaks can be indexed to pure hexagonal phase of WO_3 which agree well with JCPDS card no. 75-2187. It can be seen that the hydrothermal temperature has great effect on the crytalline size and crystallinity of the products. The diffraction peaks of samples become stronger with the raise of hydrothermal temperature (150, 180 and 210°C), while the relative intensity of diffraction peak of (200) plane weakened, instead the (001) planes increased, suggesting that both the crystalline degree and orientation of as-prepared WO_3 could be improved accordingly. That is to say, the nanoflake arrays grow along c axis and the orientation gets better along with the increasing temperature.

At the same time, the WO_3 crytalline size gradually grow smaller as shown in **Table 4.3**, which were calculated by Scherrer's equation based on (200) plane. Moreover, the crystallinity of the products becomes higher when hydrothermal temperature rises. It is known that crystal growth involves two stages: nucleation and growth. In this process, the higher the temperature reached, the more nucleation and growth would obtain, the more mature the crystals would grow. Consequently, a smaller crytalline size of WO_3 powders is obtained as the hydrothermal temperature rises (Huang et al., 2012).

Table 4.3 The crytalline size of WO_3 synthesized at different reaction temperatures

Sample Code	Heat Treatment	2Theta	D (nm)
WO_H150T20_CE	150^{o}C, 20 h	28.21	28.0
WO_H180T20_CE	180^{o}C, 20 h	28.11	22.6
WO_H210T20_CE	210^{o}C, 20 h	28.25	21.3

The SEM images of WO_H150T20_CE, WO_H180T20_CE and WO_ H210T20_CE are shown in Figure 4.7 (a-c). There appears a spot of flake like nanostructure, dominantly irregular flakes for WO_H150T20_CE, while there are a lot of regular flake like nanostructures for WO_H180T20_CE and WO_H210T20_CE. With the temperature further increasing, the well oriented WO_3 can be gained and the average diameter of nanoflakes gets larger simultaneously. That means the reaction temperature has some effect on the morphology; i.e., the higher temperature favors more flakes like nanostructures. It is known that there are two general types of chemical synthesis, i.e., kinetic control or thermodynamic control synthesis. At low temperature, the less stable kinetic product is favored because the intermediate is generated via a route that needs lower energy, while at elevated temperatures the thermodynamically stable product with higher activation energy is obtained via another intermediate. That means the flake-like nanostructures synthesized at higher temperature (180 or 210°C) are thermodynamically stable products, while the irregular flakes synthesized at lower temperature (150°C) are a less stable kinetic product in the synthesis process(Yin et al., 2012).

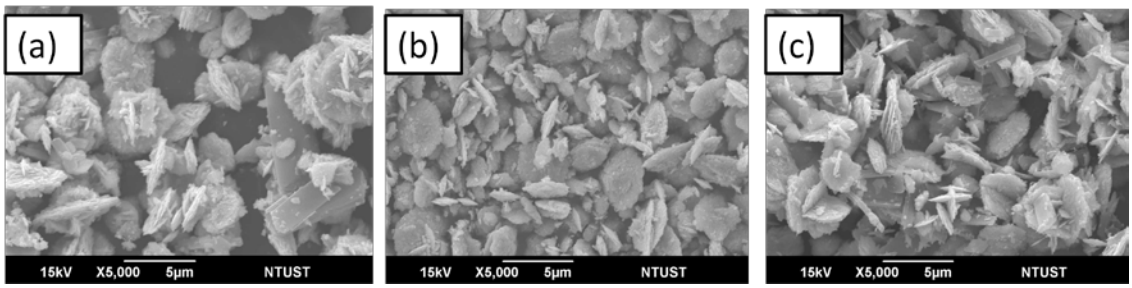

Figure 4.7 Images of WO_3 synthesized at different temperatures: (a) WO_H150T20_CE (150^{o}C), (b) WO_H180T20_CE (180^{o}C) and (c)WO_H210T20_CE (210^{o}C)

4.2.2 Electrochemical characterization of WO_3 via a NaCl & Na-EDTA-assisted hydrothermal with different reaction temperatures

Galvanostatic charge discharge performances of WO_H150T20_CE, WO_H180T20_CE and WO_H210T20_CE at a current rate of 0.1C for 1st five cycle were shown in Figure 4.8 (a), Figure 4.3 (d) and Figure 4.8 (b), respectively. In the first cycle, the discharge capacity of WO_H210T20_CE is 533.5 mAh/gr with coulombic efficiency 80.4%. Its 1st discharge capacity is higher than that of WO_H180T20_CE due to the higher crystalinity of WO_H210T20_CE. Meanwhile WO_H150T20_CE delivers discharge capacity of 692.38 with a coulombic efficiency of 44.3%, which it is lower than coulombic efficiency of WO_H180T20_CE (See **Table 4.4**). The lower 1st coloumbic capacity of WO_H150T20_CE could be resulted from incomplete reverse conversion reaction and the formation of solid electrolyte interface film.

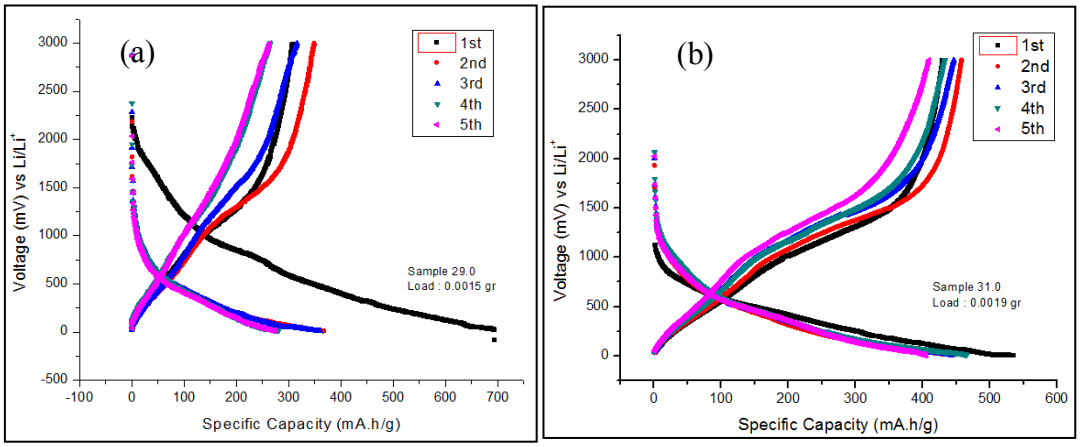

Figure 4.8 Charge/discharge curves of (a) WO_H150T20 and (b) WO_H210T20_C at a current rate of 0.1C at 1st five cycles

.

Table 4.4 First discharge capacity and coulombic efficiency of WO_3 with different reaction temperatures

Sample Code	Hydrothermal Treatment	1st discharge capacity (mAh/g)	1st coulombic efficiency (%)
WO_H150T20_CE	150°C, 20h	692.38	44.3
WO_H180T20_CE	180°C, 20h	418.50	85.3
WO_H210T20_CE	210°C, 20h	533.50	80.4

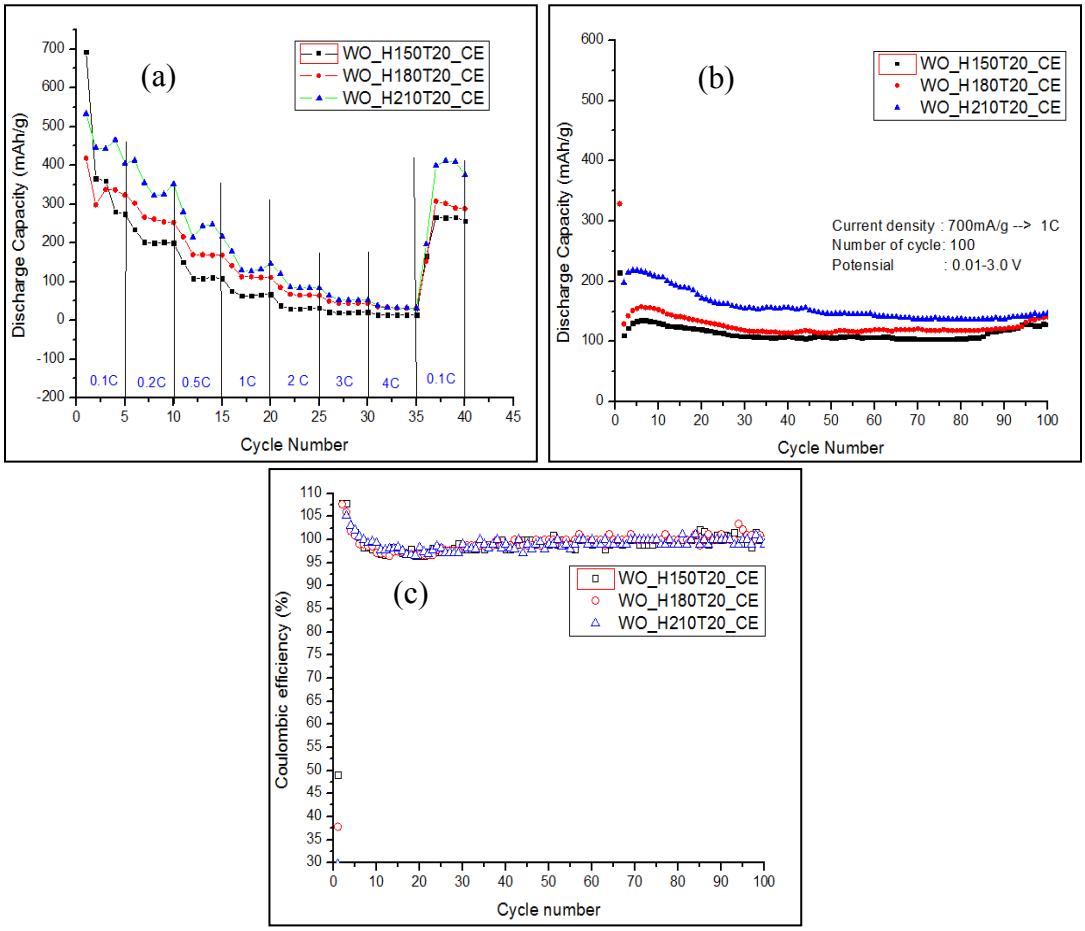

Figure 4.9 (a) Rate cycling performance with increasing current density of WO_3 synthesized at different reaction temperatures, (b) Cyclability and (c) Coulombic efficiency at current density = 700 mA/g of WO_H150T20_CE, WO_H180T20_CE and WO_H210T20_CE

The rate cycling performances of WO_H150T20_CE, WO_H180T20_CE and WO_H210T2_CE were performed at different current rate from 0.1C to 4C as shown in Figure 4.9(a). All electrodes have been discharged and charged for 5 cycles at each current rate. This measurement proved that WO_H210T20_CE has the best performance compared to WO_H150T20_CE and WO_H180T20_CE. When cycled at 0.1 C and 0.2 C, WO_H210T20_CE could delivers stable discharge capacity of 446.1 mAh/g and 355.2 mAh/g, respectively. The discharge capacity slowly decrease to 214.2, 129.3, 85.4, 52.9 and 33.5mAh/gr at current rate of 0.5, 1, 2, 3 and 4C, respectively. And then, a good capacity recovery of 399.5 mAh/g was obtained when the current rate reduced back to 0.1C.

Figure 4.9(b) and (c) illustrated the cycle life performance and coulombic efficiency of WO_H150T20_CE, WO_H180T20_CE and WO_H210T20_CE at a

current density of 700 mA/g for 100 cycles. It can seen that all of electrodes show a good stability and cyclability. The coulombic efficiency is near to 97-99% after 20 cycles. Furthermore, WO_H210T20_CE has capacity retention of 180 mAh/g after 100 cycles. It is proved that WO_H210T20_CE has the best performance compared to WO_H150T20_CE and WO_H180T20_CE.

The hydrothermal temperature has significant effect on the structure, morphology and electrochemical properties of WO_3. It has been found that the WO_3 synthesized at 210^{o}C (WO_H150T20_CE) reveals the best electrochemical properties, due to pure hexagonal phase, well grown, small crystalline size, high crystallinity and high homogeinity.

4.3 WO_3 via a NaCl & Na-EDTA-assisted hydrothermal with different Na-EDTA molar ratio

4.3.1 Material characterization of WO_3 via a NaCl & Na-EDTA-assisted hydrothermal with different Na-EDTA molar ratio

To investigate the role of EDTA in determining the phase and crystallinity of the product, WO_3 was synthesized by varying the molar ratio of Na-EDTA and keeping other parameters constant. Due to WO_H210T20_CE which be synthesized at temperature of 210^{o}C has the best performance, so in this section WO_3 products have been synthesized at temperature of 210^{o}C too. Samples with code of WO_H210T20_CE0.4, WO_H210T20_CE0.8, WO_H210T20_CE and WO_H210T20_CE1.6 are corresponded to WO_3 products which synthesized by using molar ratio of Na-EDTA to NaCl of 0.4, 0.8, 1 and 1.6, respectively.

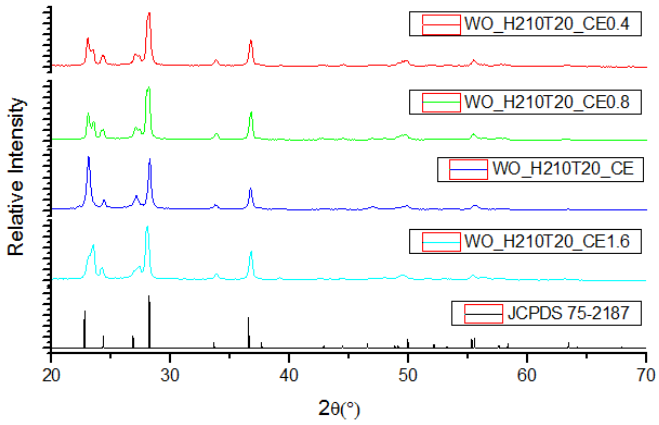

Figure 4.10 XRD pattern of WO_3 synthesized at different molar ratio of Na-EDTA to NaCl: 0.4, 0.8, 1 and 1.6

Figure 4.10 shows XRD pattern of the WO_3 samples prepared in presence of different Na-EDTA molar ratio. All the diffraction peaks are well indexed to the JCPDS card no. 751287 (h-WO_3). It is revealed from Figure 4.10 that the synthesized materials have a high intensity with sharp peaks indicating that the degree of crystallinity of WO_3 has been increased with increasing Na-EDTA concentrations. Moreover, no peaks for Na_2O were detected in XRD analysis. This suggest that EDTA plays important to control the degree of crystallinity which accordance with the literature reported (Ha et al., 2009). The crytalline size was calculated by using Scherrer's equation which leads to the average crytalline

size of 22.9, 21.4, 21.3 and 24.1 nm for WO_H210T20_CE0.4, WO_H210T20_CE0.8, WO_H210T20_CE and WO_H210T20_CE1.6, respectively (see Table 4.5).

Table 4.5 The crytalline size of WO_3 synthesized at different amount of Na-EDTA

Sample code	Heat Treatment	D (nm)	
		(001) plane	(200) plane
WO_H210T20_CE0.4	210°C, 20 h	29.1	22.9
WO_H210T20_CE0.8	210°C, 20 h	22.3	21.4
WO_H210T20_CE	210°C, 20 h	26.3	21.3
WO_H210T20_CE1.6	210°C, 20 h	12.8	24.1

Figure 4.11 shows the SEM micrographs of as synthesized WO_3 samples at different amount of Na-EDTA. It seen that the EDTA has a significant effect on the morphology, size and aggregation of the products. As seen in Figure 4.11 (a-b), the WO_3 powders (WO_H210T20_CE0.4 and WO_H210T20_CE0.8) are composed of nanoparticle which tend to aggregate. However, in high magnification, it is seen that the morphology of WO_H210T20_CE0.8 is rod like structure. Whereas, In Figure 4.11 (c-d), the nanocrystal grow up in uniform size with good aggregation and ultimately form the flake like structures for WO_H210T20_CE and WO_H210T20_CE1.6 respectively. It reveals that the WO_3 assumes the hierarchical flake-like structure composed of numerous microspheres which further composed of WO_3 nanoparticles. Moreover, it is suggest that hierarchical flake like morphology is obtained due to the effect of complexation induced by EDTA. As the concentration of EDTA increases, effect of chelation also increase that controls the aggregation of WO_3 nanoparticles and forms the hierarchical nanostructure(Adhikari et al., 2014).

Tungsten can be chelated well with EDTA and forms a stable complex of W-EDTA. The presence of sodium ion (Na^+) in EDTA plays a crucial role in modifying the morphology of the product by adsorbing oxygen quickly in the synthesis process. Thus, it appears that Na^+ based EDTA salt results self assembled tungsten oxide and provides a driving force in producing hierarchical nanostructures(Hariharan et al., 2011). During the synthesis process, W-EDTA complex is formed which gradually releases W^{6+} or W^{5+} ion to react with OH^- ion

and forms the hydrated WO_3 nanoparticles. As seen from the experiment, hydrothermal treatment temperature and EDTA concentration produce the synergy effect in determining the overall morphology of WO_3 nanostructure(Huang et al., 2012).

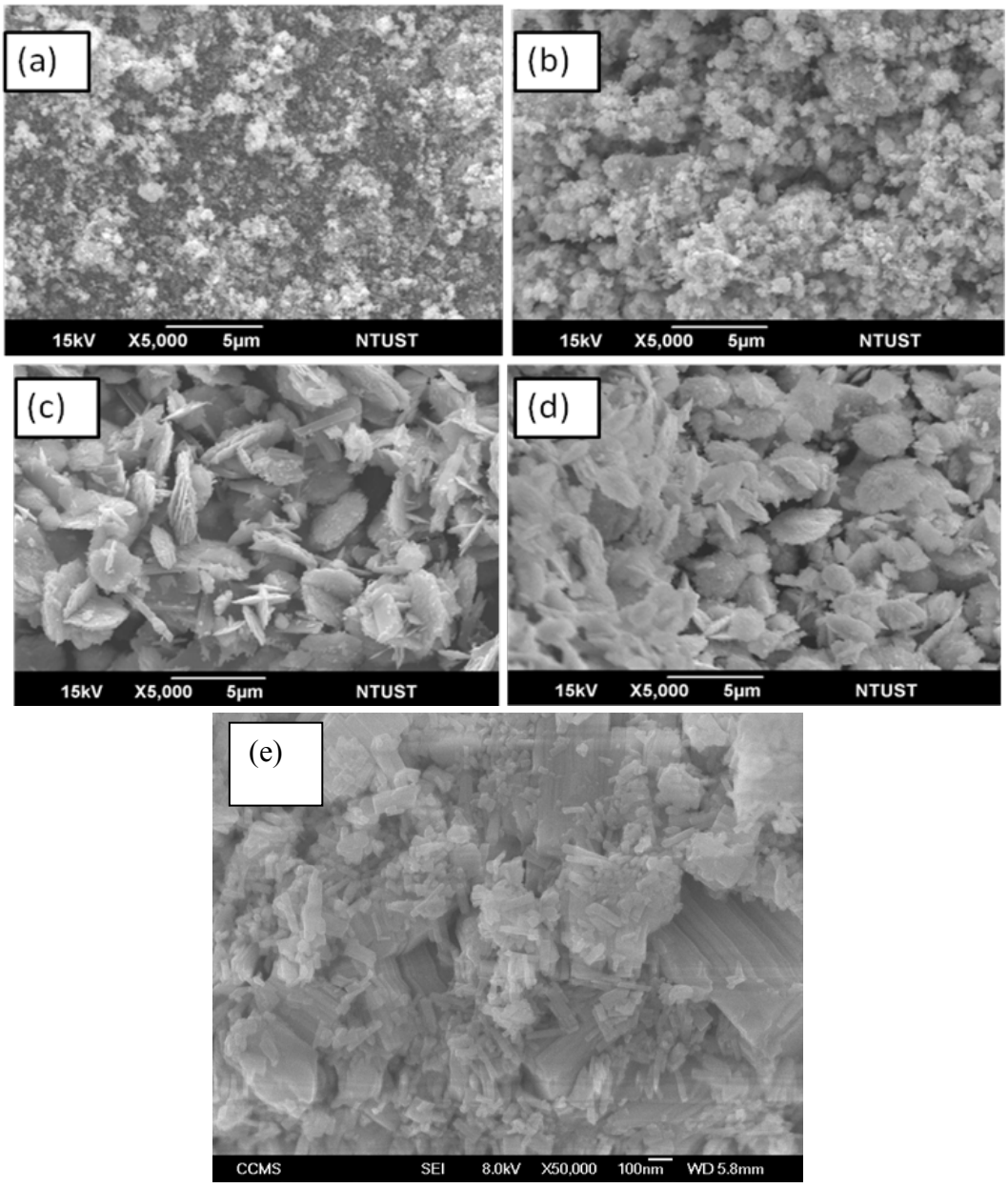

Figure 4.11 SEM Images of WO_3 synthesized at different molar ratio of Na-EDTA to NaCl: (a) WO_H210T20_CE0.4, (b) WO_H210T20_CE0.8, (c) WO_H210T20_CE, (d) WO_H210T20_CE1.6 and (e) WO_H210T20_CE0.8 (high magnification)

During the hydrothermal process, EDTA plays a vital role for the formation of hierarchical structure and the formation of hierarchical structure may be ascribed to the dissolution-recrystalization process through Ostwald ripening(Luo et al., 2005). In this process, at the expense of small crystallites, large crystallites grow by means of dissolution, diffusion and recrytalization. During the continuous hydrothermal process, these tiny particle in the presence of EDTA could dissolve and re-grow to large self assembled microspheres through Oswald ripening process (Xu et al., 2010). In the presence of higher concentration of EDTA, the microspheres thus formed further assembled to hierarchical structure through controlled aggregation(Adhikari et al., 2014).

4.3.2 Electrochemical characterization of WO_3 via a NaCl & Na-EDTA-assisted hydrothermal with different Na-EDTA molar ratio

Figure 4.12(a), Figure 4.12(b), Figure 4.8(b) and Figure 4.12(c) show the galvanostatic charge discharge at 1st five cycles at a current rate of 0.1C for WO_H210T20_CE0.4, WO_H210T20_CE0.8, WO_H210T20_CE and WO_H210T20_CE1.6, respectively. The electrochemical performance evaluation of the samples can be seen in **Table 4.4**. WO_H210T20_CE0.4 electrode delivers discharge capacity of 767.1 mAh/g with a coulombic efficiency of 58.7% in the first cycle. Particularly, the irreversible capacity in first cycle could be resulted from incomplete reverse conversion reactions and the formation of solid electrolyte interface film (Xiao et al., 2013). In other hand, the first discharge capacity of WO_H210T20_CE0.8 is 558.93 mAh/g, with a high coulombic efficiency of 86.9% which is higher than that of others electrodes. Importanly, the higher first coulombic efficiency for WO_H210T20_CE0.8 could be due to the smaller particle size of WO_3 and the lower surface area of WO_3.

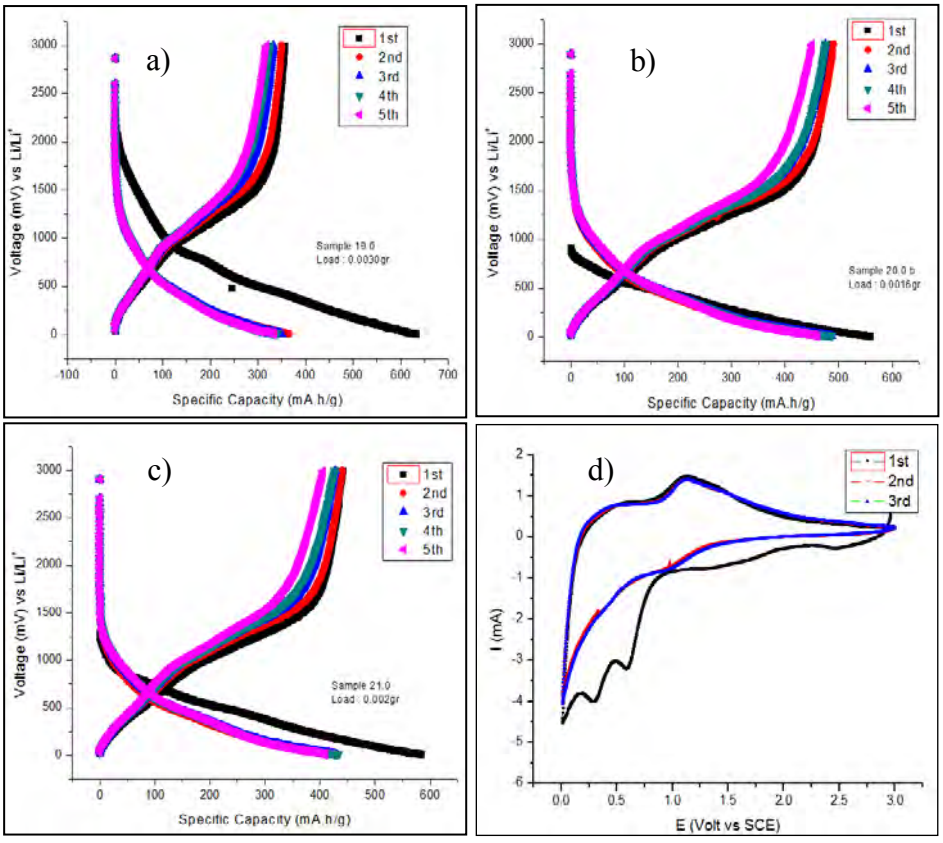

Figure 4.12 Charge/discharge curves of (a) WO_H210T20_CE0.4, (b) WO_H210T20_CE0.8, and (c) WO_H210T20_CE1.6 at a current rate of 0.1C. (d) Cyclic voltammetry of WO_H210T20_CE0.8

Table 4.6 First discharge capacity and coulombic efficiency of WO_3 with different Na-EDTA molar ratio

Sample Code	Hydrothermal Treatment	1st discharge capacity (mAh/g)	1st coulombic efficiency (%)
WO_H210T20_CE0.4	210°C, 20h	767.10	58.70
WO_H210T20_CE0.8	210°C, 20h	558.93	86.90
WO_H210T20_CE	210°C, 20h	533.50	80.37
WO_H210T20_CE1.6	210°C, 20h	582.86	75.74

Cyclic voltammetry of WO_H210T20_CE0.8 based electrode was recorded between 0.01 and 3.0 V and are shown in Figure 4.12(d). For the first cycle, in the cathodic polarization process, a strong reduction peak at 0.6 V and 0.3 V (vs Li^+/Li) were observed; while in the following anodic polarization, only one broad oxidation peak with peak maximum at 1.1 V was observed. However, during the second cycle, only one broad reduction peak was noticed at about 0.97 V and the other reduction peak that appeared in the first cycle disappeared completely, whereas the anodic polarization process showed only one broad peak centered at 1.1 V. The pair of peaks at 0.97 V (cathodic sweep) and 1.1 V (anodic sweep) indicate the reversible lithium insertion and deinsertion processes. The disappearance of cathodic peak at 0.6 and 0.3 V indicates some irreversible lithium insertion into the crystal structure, which is believed to be caused by unrecoverable phase transformation, leading to irreversible capacity loss(Sasidharan et al., 2012).

The rate cycling performance of as-synthesized WO_3 with different Na-EDTA molar ratio at different current rates is shown in Figure 4.13(a). In generally, the discharge/charge capacities decrease with increase of current rates similar to other electrodes. As shown in Figure 4.13 (a), WO_H210T20_CE0.8 exhibits much higher specific capacities than others electrode at all investigated charge discharge rates. WO_H210T20_CE0.8 constructed electrode deliver discharge capacities of 483.9, 422.3, 272.3, 170.5, 101.8, 71.4 and 56.2 mAh/g during the second cycle as the current rates vary from 0.1C to 4C. With gradually increasing the current rate, the capacity drops steadily but the electrode regains its

original capacity when the rate was again lowered to 0.1 C (405.4 mAh/g). In contrary, WO_H210T20_CE0.4 faded rapidly during increasing the current rate.

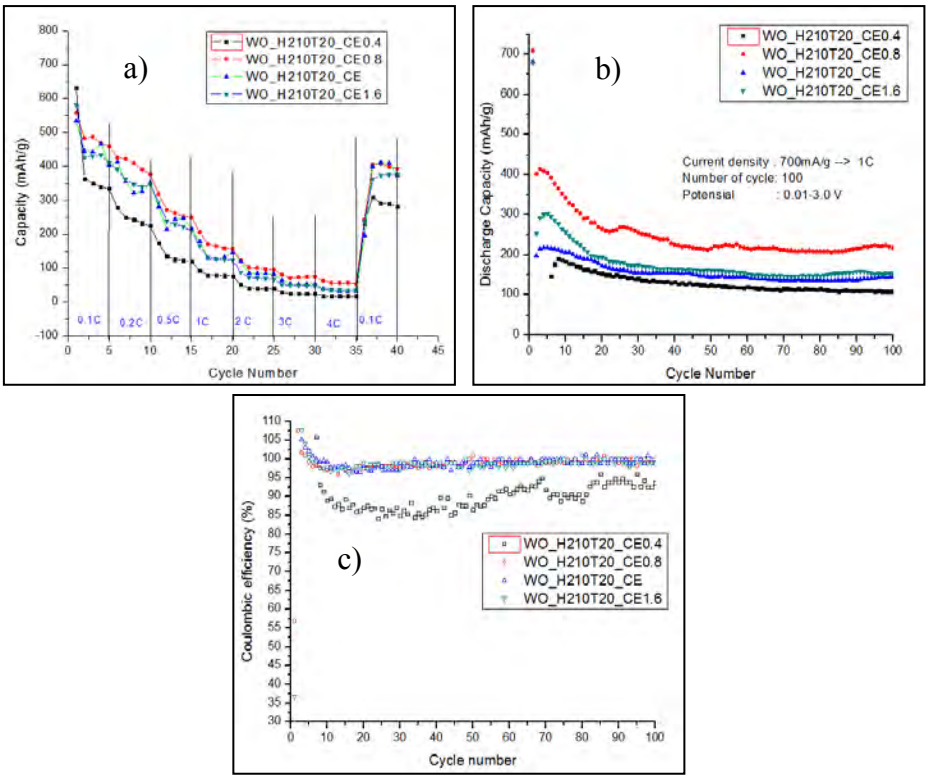

Figure 4.13 (a) Rate cycling performance of WO_3 synthesized at different Na-EDTA molar ratio with increasing current density, (b) Cyclability and (c) coulombic efficiency at current density = 700 mA/g of WO_H210T20_CE0.4, WO_H210T20_CE0.8, WO_H210T20_CE and WO_H210T20_CE1.6

Figure 4.13(b) and (c) exhibit cycling life performance and coulombic efficiency of as-synthesized WO_3 with different Na-EDTA molar ratio up to 100 cycles of repeated discharge/charge at a current density of 700mAh/g in the voltage window 0.01-3.0 V (vs. Li^+/Li). The discharge-charge capacities decrease gradually that it is more pronounced in the first few cycles. This phenomenon is attributed to the formation of stable electrolyte films and complete coverage and structural organization of nanospheres may require several cycles of charge/discharges (Sasidharan et al., 2012). WO_H210T20_CE0.8 has the best performance which the initial discharge capacity of 708.5 mAh/g and the capacity retention of 218.1 mAh/g after 100 cycles. The coulombic efficiency after 20 cycles is more than 97% hence it suggests that the electrodes are highly stable during lithium insertion and extraction kinetics.

4.4 WO_3/rGO via a hydrothermal method with different amount of graphene oxide

4.4.1 Material characterization of WO_3/rGO via a hydrothermal method with different amount of graphene oxide

To enhance the electrochemical performance, graphene oxide was introduced into synthesis of WO_3. WO_3/rGO was synthesized by using hydrothermal method at different amount of graphene oxide. The weight persen of GO were 4%, 6% and 8%, which corresponding WO_3/graphene samples were donated as WO_H180T20_GO4%, WO_H180T20_GO6% and WO_H180T20_GO8%, respectively.

Figure 4.14 shows the XRD patterns of the as-synthesized products at 180^{o}C for 20 h with different amount of GO. All the diffraction peaks also can be perfectly indexed to hexagonal tungsten oxide crystalline phase (h-WO_3) with the space group P6/mmm (JCPDS 75-2187). No obvious diffraction peaks of rGO can be observed due to the strong signal from WO_3. It can be seen that the rGO content has no influence on the crystal structure of WO_3.

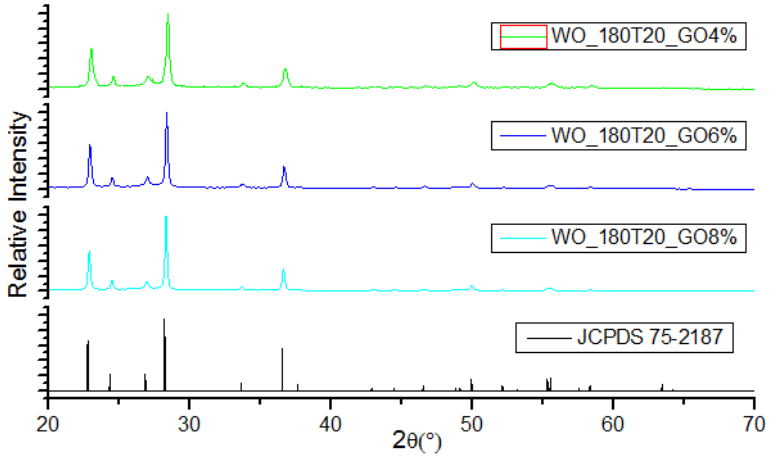

Figure 4.14 XRD pattern of WO_3/graphene synthesized at different amount of graphene oxide

The characteristic absorption peaks of WO_3 are also revealed in the XRD pattern of WO_3/rGO, demonstrating the formation of WO_3 on surface of rGO without impurities. And the increase of grain size match positively with decreasing mass ratio of WO_3 to rGO, which may be ascribed to the increasing amount of rGO in WO_3/graphene composites. rGO has contribution for the formation of particles. The higher rGO content, the bigger crytalline size like shown in Table 4.7. below.

Table 4.7 The crystalline size of WO_3/rGO synthesized at different amount of GO

Sample no.	Heat Treatment	2θ	D (nm)
WO_H180T20_GO4%	180°C, 20 h	28.44	36.2
WO_H180T20_GO6%	180°C, 20h	28.36	43.9
WO_H180T20_GO8%	180°C, 20h	28.32	48.5

The Raman spectra of WO_3/rGO composites with different amount of GO is shown in Figure 4.15. Raman Scattering peaks observed at 676.1 cm^{-1} and 807.7 cm^{-1} refer to O-W-O stretching mode and these bands can be assigned to the fundamental mode of crystalline h-WO_3(Ha et al., 2009). Whereas peak at 945.3 cm-1 refer to W=O stretching mode of terminal oxygen atoms that are present on the surface of the cluster (dagling bond) or at the bounderies of nanometer grains(Huirache-Acuña et al., 2009). Furthermore, all WO_3/rGO samples display peaks at which are in good correspondence with disordered (D) band and graphitic (G) band of graphene(Xiao et al., 2013). With the increasing amount of rGO in composite, the intensity of peaks corresponding to WO_3 is decreasing comparing to that of D and G band.

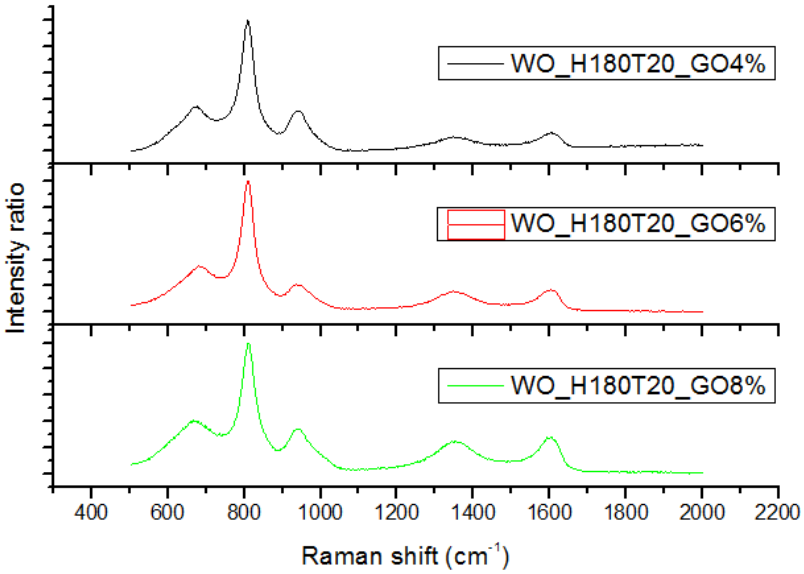

Figure 4.15 Raman Spectra of as-synthesized WO_3 with different amount of graphene oxide

To calculate the mass ratio of WO_3 to rGO, TG analysis is conducted from temperature of 100°C to 900°C at heating rate of 10°C/minute in air atmosphere.

In Figure 4.16, the mayor weight loss appeared between 400°C and 550°C is resulted from decomposition of rGO. And rGO content in samples of WO_H180T20_GO4%, WO_H180T20_GO6% and WO_H180T20_GO8% are 4.6%, 5.8% and 8.1%, respectively.

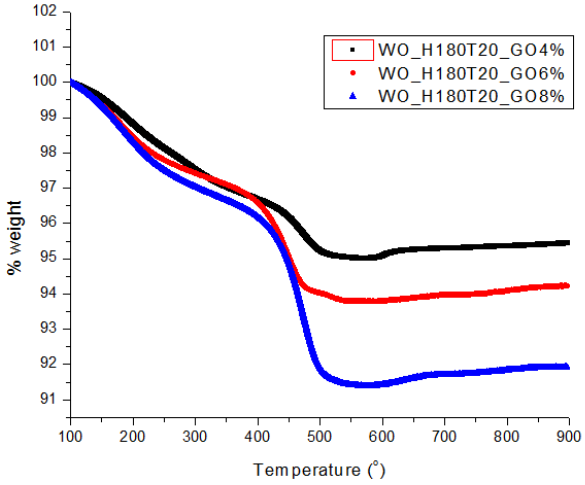

Figure 4.16 TGA curves of (a) WO_H180T20_GO4%, (b) WO_H180T20_GO6% and (c) WO_H180T20_GO8%

Figure 4.17 shows the morphologies and structures of WO_3/rGO composites with different GO composition. While the average crytalline size of the WO_3 is all about 0.5 µm, the amount of WO_3 embedded into rGO change as content of rGO changes. And the rGO could effectively prevent the aggregation of WO_3 particles and disperse them uniformly. The studies in the literature indicate that the introduction of rGO in the composite is helpful to suppress the aggregation and hindering the growth of nanoparticles to a certain extent, possibly due to the partition effect of the graphene (Rai et al., 2012). The small particles sizes are a key to enhance the electrochemical performances because it shortens the distance of Li^+ ion diffusion in the solid phase. The nanoparticles are anchored on the surface of rGO with a high density, and they facilitate rapid electron transport between the underlying graphene nanosheets. It is also reasonable to suggest that the random hybridization between nanoparticles and graphene can form 3-D porous structure of the nanocomposite, which is beneficial for achieving high rate performances (Rai et al., 2013a).

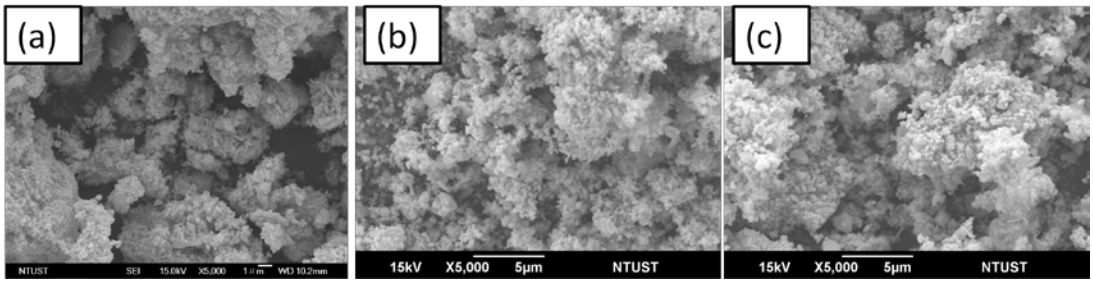

Figure 4.17 SEM images of (a) WO_H180T20_GO4%, (b) WO_H180T20_GO6% and (c) WO_H180T20_GO8%

4.4.2 Electrochemical characterization of WO_3/rGO via a hydrothermal method with different amount of graphene oxide

Fig. 4.2 (a–c) shows the charge/discharge curves of WO_H180T20_GO4%, WO_H180T20_GO6% and WO_H180T20_GO8%, respectively, for 1st, 2nd and 3rd cycle at 0.1 C between 3.0V and 0.01V (vs. Li/Li^+). The first discharge of WO_H180T20_GO4% is 635 mAh/g with a coloumbic efficiency of 64.8% and WO_H180T20_GO6% exhibits first discharge of 832.3 mAh/g with a coloumbic efficiency of 63.8%. While The first discharge of WO_H180T20_GO8% is 987.4 mAh/g with a coloumbic efficiency of 64.6% (see Table 4.8). Particularly, the irreversible capacity loss in first cycle could be resulted from incomplete reverse conversion reactions and the formation of solid electrolyte interface film. The higher first cycle columbic efficiency could be attributable to good attachments between rGO and WO_3.

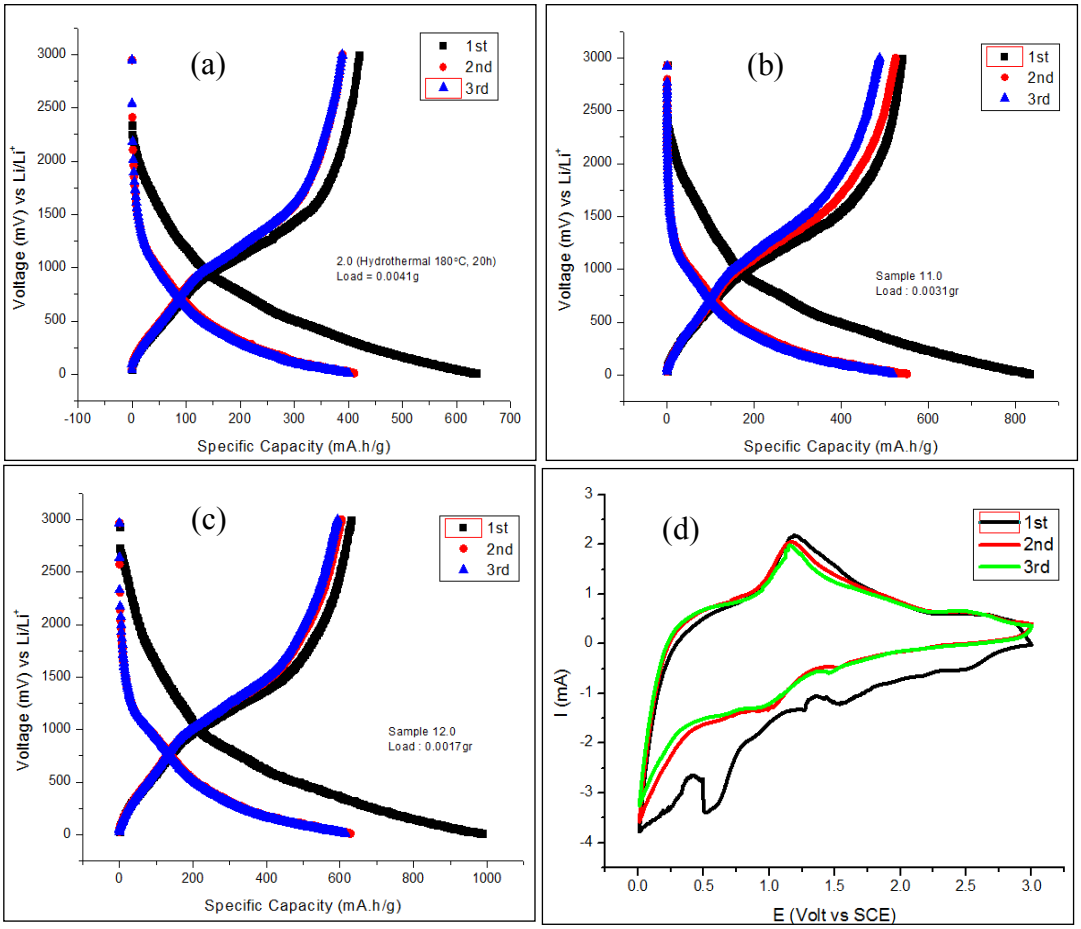

Figure 4.18 Charge/discharge curves of (a) WO_H180T20_GO4%, (b) WO_H180T20_GO6% and (c) WO_H210T20_GO8% at a current rate of 0.1C. (d) Cyclic voltammetry of WO_H210T20_GO4%.

Importantly, as the theoretical capacity of WO_3 is only 693 mAh/gr, the higher discharge capacity of WO_3/rGO could be not only resulted from decomposition of electrolyte in lower potential region, but also from electrochemical reduction of some remained oxygen-containing functional groups on the surface of reduced graphene oxide. Meanwhile, positive interaction between rGO and WO_3, accessible sites on rGO to insert/extract Li ion as well as interfacial lithium storage reactions occurring at surface of WO_3 or rGO, contribute to the extra charge capacity(Xiao et al., 2013).

Table 4.8 First discharge capacity and coulombic efficiency of WO_3 with different amount of graphene oxide

Sample Code	Hydrothermal Treatment	1st discharge capacity (mAh/g)	1st coulombic efficiency (%)
WO_H180T20_GO4%	180°C, 20h	635.8	64.6
WO_H180T20_GO6%	180°C, 20h	832.3	64.8
WO_H180T20_GO8%	180°C, 20h	987.4	63.8

Figure 4.18 (d) shows CV of WO_H180T20_GO4% electrode at 1st three cycles. At first cycle, this electrode exhibits three cathodic peaks at 1.5, 1.2 and 0.5 V and one main anodic peak at 1.2 V, which are corresponding to the extraction and insertion of lithium ions along with the formation of amorphous Li_2O and a partially irreversible SEI layer on the surface of the nanoparticles. However, these peaks can be attributed to the multistep reversible electrochemical reactions between WO_3 and W/Li_2O (e.g. $WO_3 + 6Li^+ + 6e^- \leftrightarrow 3Li_2O + 3W^0$) and reversible oxidation of metal tungsten to tungsten oxide, respectively. In addition, all the peaks were absent from the second cycle. From the second cycle, the reduction peak shifted to 1 V, which was possibly related to the insertion of Li^+ ions into the nanocomposite at different stages (Rai et al., 2013b). The pair of cathodic peak at 1 V and anodic peak at 1.2 V after second cycle indicates the reversible capacity of WO_3.

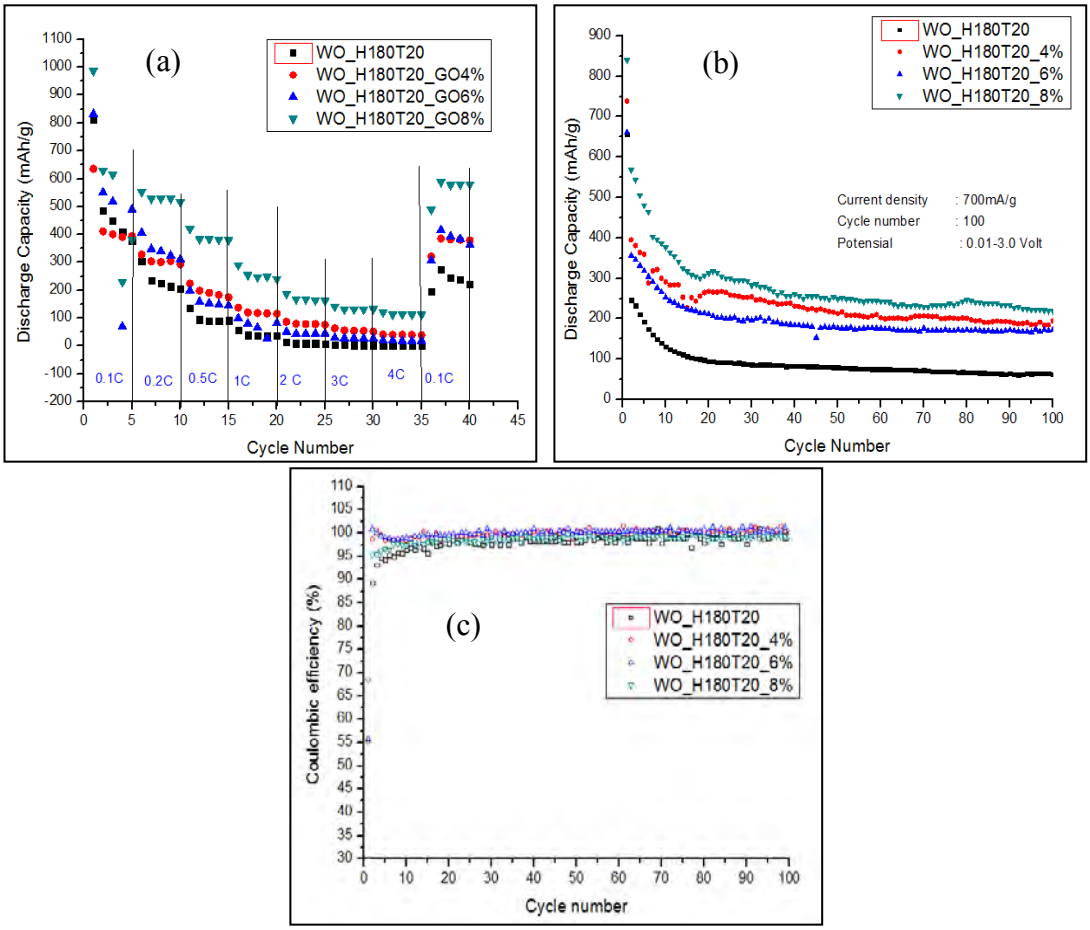

Figure 4.19 (a) Rate cycling performance with increasing current density of WO_3/graphene synthesized at different amount of graphene oxide, (b) Cyclability and (c) coulombic efficiency at current density = 700 mA/g of WO_H180T20, WO_H180T20_GO4%, WO_H180T20_GO6% and WO_H210T20_GO8%

The rate cycling performances of WO_H180T20_GO4%, WO_H180T20_GO6% and WO_H180T20_GO8% which be compared with bare WO_3 (WO_H180T20) are shown in Figure 4.19 (a). These are performed at different current rate from 0.1C to 4C (1C = 693 mA/gr) between 3.0V and 0.01V (vs. Li/Li^+) for 5 cycles for each current rate. The capacity of bare WO_3 (WO_H180T20) fades rapidly and cannot recover to initial specific capacity values when reverting back to lower charge/discharge currents following cycling at high current rates. On the contrary, when the testing currents are regularly returned to a lower rate, the discharge capacities for WO_H180T20_GO4%, WO_H180T20_GO6% and WO_H180T20_GO8% electrodes could be recovered

to approximately the initial capacity values. This result indicates that the WO_3/rGO material present the excellent structure stability. That means the capacity retention of WO_3/rGO is excellent due to the structure of material which can storage more lithium.

Figure 4.19 (c) and (d) show cycle life performance and coulombic efficiency of WO_H180T20, WO_H180T20_GO4%, WO_H180T20_GO6% and WO_H180T20_GO8% at current density of 700mAh/g for 100 cycles. The discharge capacity of WO_H180T20 electrode decreased significantly and is equal to 62.5 mAh/g after 100 cycles. On the contrary, after 100 cycles the discharge capacity of WO_H180T20_GO4%, WO_H180T20_GO6% and WO_H180T20_GO8% electrodes delivered as high as 194.7, 172.5 and 219.5 mAh/g, repectively, indicating excellent electrochemical performance. Furthermore, all of electrodes show good coulombic efficiency. After 20 cycles, they can reach a coulombic efficiency of 96% or higher. The enhancement of reversible lithium storage may be synergistic in nature arising from the electronic interactions involving rGO and WO_3(Shiva et al., 2013).

The good structure stability of the WO_3/rGO composites, its superior rate and cycle performance are also resulted from the enhanced electronic conductivity, shortening lithium ion diffusion distance, as well as decreasing inner resistance of lithium ion batteries via effective combination of rGO and WO_3 for composite(Shiva et al., 2013).

For further investigation of electrochemical properties, some WO_3 based electrodes were conducted cycle life test at current rate of 0.2 C. Figure 4.20 shows cycle life performance of WO_3 based anode material with different composition and heat treatment at current rate of 0.2 C for 50 cycles. The bare WO_3 electrode (WO_H180T20) fades rapidly upon cycling. The discharge capacity decrease to only 127.1 mAh/g after 50 cycles due to the severe pulverization. In other hand, WO_3/rGO electrode (WO_H180T20_GO4%) exhibits better cycling performance and reversibility which delivers a discharge capacity of 347.5 mAh/g after 50 cycles. The enhancement lithium storage capacity of electrode is related to the synergistic effect between WO_3 and rGO, resulting in the decrease of the irreversible capacity of WO_3. In second position,

WO_H210T20_CE delivered a discharge capacity of 301.7 mAh/g after 50 cycles. It demonstrating that the nanosized particles are able to expand much more easily and have better accommodation of the structural strain for electrochemical reasction of lithium, resulting in improving cycle life(Gu et al., 2007).

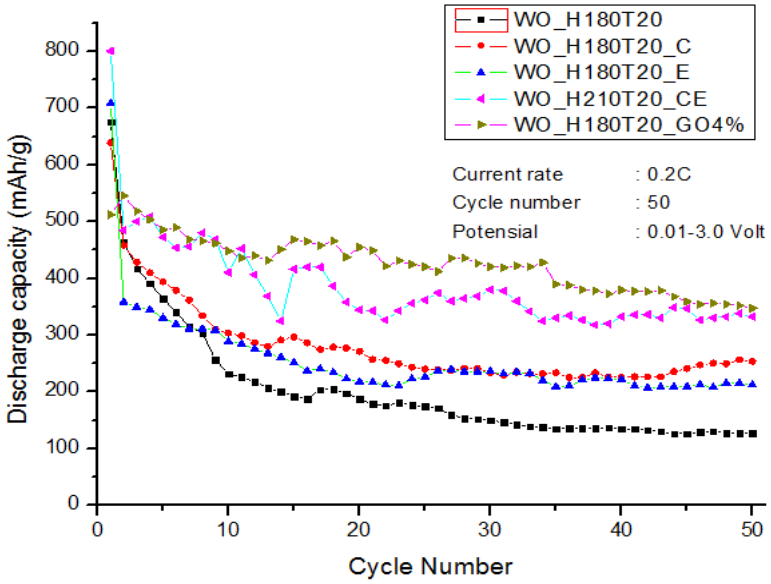

Figure 4.20 Cycle life performance of WO_3 based anode materials with different composition and heat treatment at current rate of 0.2 C for 50 cycles

(This page is empty deliberately)

CHAPTER 5
CONCLUSIONS AND SUGGESTIONS

5.1 Conclusions

Hexagonal tungsten trioxide (h-WO_3) with improved reversible capacity and cyclic stability has been successfully synthesized via hydrothermal method using different sodium salts. The morphologies of WO_3 were obtained are nanoparticle (WO_H180T20 and WO_H180T20_C) and flake like nanostructure (WO_H180T20_E and WO_H180T20_CE). Compared to others, WO_H180T20_CE has the best electrochemical performance owing to its good homogeneity, high crystallinity and small grain size. It can be attributed to the effect of NaCl and Na-EDTA. WO_H180T20_CE electrode delivers discharge capacity of 418.50 mAh/g with a coulombic afficiency of 85.3% at the first cycle at a current rate of 0.1 C. Furthermore, it remains 150 mAh/g after 100 cycles at a current density of 700 mA/g.

Synthesis of WO_3 via NaCl and NaEDTA assisted hydrothermal with different temperatures have been carried out. All of samples morphologies are flake like nanostructure. As the reaction temperature was increased, the crystallinity of WO_3 also increased. It has been found that the WO_3 synthesized at 210^{o}C (WO_H150T20_CE) reveals the best electrochemical properties, which obtain pure hexagonal phase, well grown, small crystalline size, high crystallinity and high homogeinity. The discharge capacity of WO_H210T20_CE is 533.5 mAh/gr with a coulombic efficiency of 80.4% at first cycle. Furthermore, WO_H210T20_CE has a capacity retention of 180 mAh/g after 100 cycles at current density of 700 mA/g.

Subsequently, WO_3 was synthesized by varying the molar ratio of Na-EDTA to investigate the role of EDTA in determining the phase and crystallinity of the product. The different EDTA molar ratio, the different morphology was obtained. The morphologies of WO_H210T20CE0.4 and WO_H180T20_CE0.8 with NaEDTA molar ratio of 0.4 and 0.8 are nanoparticle and rod-like structure, respectively. On the other hand, WO_H210T20CE and WO_H210T20CE1.6 with NaEDTA molar ratio of 1 and 1.6, the nanocrystal grow up in uniform size with

good aggregation and ultimately form the flake like structures. WO_H180T20_CE0.8 has the best electrochemical performances. Its electrode delivers discharge capacity of 558.93 mAh/g with a high coulombic efficiency of 86.9%. Moreover, this electrode has capacity retention of 218.1 mAh/g after 100 cycles at a current density of 700 mA/g due to the hierarchical nanostructure and lower surface area of WO_3.

In the last part, WO_3/rGO was synthesized by using hydrothermal method at different amount of graphene oxide to enhance its electrochemical performance. The rGO could effectively prevent the aggregation of WO_3 particles and disperse them uniformly. The first discharge of WO_H180T20_GO8% is 987.4 mAh/g with a coloumbic efficiency of 64.6% due to good attachments between rGO and WO_3. Furthermore, at a current density of 700 mA/g the discharge capacity of WO_H180T20_GO8% electrode delivers as high as 219.5 mAh/g after 100 cycles, indicating excellent electrochemical performance. The good structure stability of the WO_3/rGO, its superior rate and cycle performance are resulted from the enhanced electronic conductivity, shortening lithium ion diffusion distance, as well as decreasing inner resistance of lithium ion batteries via effective combination of rGO and WO_3.

This work proved that WO_3 based anode materials exhibit a high reversible capacity, excellent cycling performance and remarkable rate capability when used as anode electrode materials for lithium ion batteries.

5.2 Suggestions

There are some suggestions for the next work about synthesis WO_3 based anode materials for lithium ion battery, such as:

1. Introducing graphene into synthesis of WO_3 via a NaCl and Na-EDTA assisted hydrothermal to improve its discharge capacity and rate capability.
2. Optimizing the amount of graphene oxide added to WO_3/graphane.

3. Adding sulfate ion like Na_2SO_4 to enhance the one dimensional growth of the final product. Na_2SO_4 also play important role in the formation of self assembled nanostructures.
4. Optimizing the reaction temperature because it looks that the higher temperature shows better performances

(This page is empty deliberately)

ENCLOSURE

A. Theoritical Capacity of Materials for Battery Anode

The theoretical capacity of a battery is the quantity of electricity involved in the electrochemical reaction. It is denoted Q and is given by:

$$Q = xnF$$

where x = number of moles of reaction, n = number of electrons transferred per mole of reaction and F = Faraday's constant (96500 C/mol)

The capacity is usually given in terms of mass, not the number of moles:

$$Q = \frac{nF}{M_r}$$

where M_r = Molecular Mass. This gives the capacity in units of mili-Ampere hours per gram (mAh/g).

Example: Calculate Theoritical capacity of WO_3:

According to the following conversion reaction mechanism:

$$WO_3 + 6Li^+ + 6e^- \leftrightarrow W + 3Li_2O$$

So,

n = 6

F = 96500 C/mol

Mr = 232 gr/mol

***Theoritical capacity of WO_3 $\rightarrow Q = \frac{6 \text{ x } 96500 \text{ C/mol}}{232 \text{ gr/mol}} = 2297.62 \text{ C/gr}$

Because I mAh =3.6 C, so 2297.62 C/g = **638.23 mAh/gr**

B. Current rate (C_{rate})

C_{rate} is the current amount which applied in an electrode during charging or discharging**.** 1 C means that for charging or discharging a sample in one hour, we apply a positive or negative current that is equivalent to the capacity of the material. It means that we will charge a battery to full capacity in one hour. A battery performs best if it is charged and discharged slowly. If a battery is charged too quickly, then it will be hindered from reaching full capacity. The reason for this is that upon charging and discharging, there is reduction/oxidation going on both at the anode and cathode, this means there is literally a structural transition happening. If a battery is charged too quickly not all of the material will release Li+ or will not undergo the proper structural transition.

In this work, the batteries were charged at 1C, so it should take one hour to charge each battery and it should take one hour to discharge each battery. However, we will find that the battery actually took less than one hour to charge, and less than one hour to discharge.

Example: a WO_3 electrode with loading of 10 mg=0.01 g would be charged at I C (h^{-1}), so the current should be applied is :

$$I = 0.01 \text{ x } 693 \text{ mAh x } 1 \text{ } h^{-1} = 6.93 \text{ mA}$$

C. Coulombic efficiciency

Coulombic efficiency is the comparison between charge capacity to discharge capacity in the same cycle multipled by 100%. In the first cycle, an electrode has discharge capacity of D and charge capacity of C, so its coulombic efficiency (E) is:

$$\mathrm{E} = \frac{C}{\mathrm{D}} \mathrm{x}\, 100\%$$

Example :

WO_3 electrode has discharge capacity of 600 mAh/gr with charge capacity of 400 mAh/gr in the 1st cycle, So its coulombic efficiency is:

$$E = \frac{400}{600} x\, 100\% = 66.67\ \%$$

(This page is empty deliberately)

REFERENCES

ADHIKARI, R., GYAWALI, G., SEKINO, T. & WOHN LEE, S. 2014. EDTA mediated microwave hydrothermal synthesis of WO_3 hierarchical structure and its photoactivity under simulated solar light. *Journal of Environmental Chemical Engineering*.

BAKER, A., HODGSON, S. & EDIRISINGHE, M. 2002. Production of tungsten oxide coatings, via sol–gel processing of tungsten anion solutions. *Surface and Coatings Technology,* 153**,** 184-193.

BATHE, S. R. & PATIL, P. 2009. Electrochromic characteristics of pulsed spray pyrolyzed polycrystalline WO3 thin films. *Smart Materials and structures,* 18**,** 025004.

BECERRIL, H. A., MAO, J., LIU, Z., STOLTENBERG, R. M., BAO, Z. & CHEN, Y. 2008. Evaluation of solution-processed reduced graphene oxide films as transparent conductors. *ACS nano,* 2**,** 463-470.

BERGER, C., SONG, Z., LI, X., WU, X., BROWN, N., NAUD, C., MAYOU, D., LI, T., HASS, J. & MARCHENKOV, A. N. 2006. Electronic confinement and coherence in patterned epitaxial graphene. *Science,* 312**,** 1191-1196.

BOBLETER, O. 1994. Hydrothermal degradation of polymers derived from plants. *Progress in Polymer Science,* 19**,** 797-841.

BUDAVARI, S., O'NEIL, M., SMITH, A. & HECKELMAN, P. 1989. The merck index: an encyclopedia of chemicals, drug, and biologicals.

CAI, D., WANG, S., LIAN, P., ZHU, X., LI, D., YANG, W. & WANG, H. 2013. Superhigh capacity and rate capability of high-level nitrogen-doped graphene sheets as anode materials for lithium-ion batteries. *Electrochimica Acta,* 90**,** 492-497.

CHEN, B.-D., PENG, C.-X. & CUI, Z. 2012. Ultrasonic synthesis of CoO/graphene nanohybrids as high performance anode materials for lithium-ion batteries. *Transactions of Nonferrous Metals Society of China,* 22**,** 2517-2522.

CHEN, D., GAO, L., YASUMORI, A., KURODA, K. & SUGAHARA, Y. 2008. Size-and Shape-Controlled Conversion of Tungstate-Based Inorganic–Organic Hybrid Belts to WO_3 Nanoplates with High Specific Surface Areas. *Small,* 4**,** 1813-1822.

CHEN, X. & M AO, S. S. 2007. Titanium dioxide nanomaterials: synthesis, properties, modifications, and applications. *Chemical reviews,* 107**,** 2891-2959.

DE LAS CASAS, C. & LI, W. 2012. A review of application of carbon nanotubes for lithium ion battery anode material. *Journal of Power Sources,* 208**,** 74-85.

DING, Y., JIANG, Y., XU, F., YIN, J., REN, H., ZHUO, Q., LONG, Z. & ZHANG, P. 2010. Preparation of nano-structured $LiFePO_4$/graphene composites by co-precipitation method. *Electrochemistry Communications,* 12**,** 10-13.

DONG, H., LIU, Y., YANG, P., WANG, W. & LIN, J. 2010. Controlled synthesis and characterization of $LaPO_4$, $LaPO_4$: Ce^{3+} and $LaPO_4$: Ce^{3+}, Tb^{3+} by EDTA assisted hydrothermal method. *Solid state sciences,* 12**,** 1652-1660.

DREYER, D. R., PARK, S., BIELAWSKI, C. W. & RUOFF, R. S. 2010. The chemistry of graphene oxide. *Chemical Society Reviews,* 39**,** 228-240.

FELIX. 2012. *Investigation on Novel Sulfured-Based Additives for Solid Electrolyte Interface (SEI) Improver in High Voltage Lithium Ion Battery Application.* Master, National taiwan University of Science and Technology.

FERNANDEZ-MERINO, M., GUARDIA, L., PAREDES, J., VILLAR-RODIL, S., SOLIS-FERNANDEZ, P., MARTINEZ-ALONSO, A. & TASCON, J. 2010. Vitamin C is an ideal substitute for hydrazine in the reduction of graphene oxide suspensions. *The Journal of Physical Chemistry C,* 114**,** 6426-6432.

GARROTE, G., DOMINGUEZ, H. & PARAJO, J. 1999. Hydrothermal processing of lignocellulosic materials. *European Journal of Wood and Wood Products,* 57**,** 191-202.

GEIM, A. K. & NOVOSELOV, K. S. 2007. The rise of graphene. *Nature materials,* 6**,** 183-191.

GORIPARTI, S., MIELE, E., DE ANGELIS, F., DI FABRIZIO, E., PROIETTI ZACCARIA, R. & CAPIGLIA, C. 2014. Review on recent progress of nanostructured anode materials for Li-ion batteries. *Journal of Power Sources*.

GU, Z., LI, H., ZHAI, T., YANG, W., XIA, Y., MA, Y. & YAO, J. 2007. Large-scale synthesis of single-crystal hexagonal tungsten trioxide nanowires and electrochemical lithium intercalation into the nanocrystals. *Journal of Solid State Chemistry,* 180**,** 98-105.

GU, Z., MA, Y., YANG, W., ZHANG, G. & YAO, J. 2005. Self-assembly of highly oriented one-dimensional h-WO3 nanostructures. *Chemical communications***,** 3597-3599.

HA, J.-H., MURALIDHARAN, P. & KIM, D. K. 2009. Hydrothermal synthesis and characterization of self-assembled h-WO3 nanowires/nanorods using EDTA salts. *Journal of Alloys and Compounds,* 475**,** 446-451.

HAM, D. J., PHURUANGRAT, A., THONGTEM, S. & LEE, J. S. 2010. Hydrothermal synthesis of monoclinic WO_3 nanoplates and nanorods used as an electrocatalyst for hydrogen evolution reactions from water. *Chemical Engineering Journal,* 165**,** 365-369.

HARI KRISHNA, R., NAGABHUSHANA, B. M., NAGABHUSHANA, H., CHAKRADHAR, R. P. S., SIVARAMAKRISHNA, R., SHIVAKUMARA, C. & THOMAS, T. 2014. Auto-ignition based synthesis of Y2O3 for photo- and thermo-luminescent applications. *Journal of Alloys and Compounds,* 585**,** 129-137.

HARIHARAN, V., PARTHIBAVARMAN, M. & SEKAR, C. 2011. Synthesis of tungsten oxide ($W_{18}O_{49}$) nanosheets utilizing EDTA salt by microwave irradiation method. *Journal of Alloys and Compounds,* 509**,** 4788-4792.

HEINDORFF, K., AURICH, O., MICHAELIS, A. & RIEGER, R. 1983. Genetic toxicology of ethylenediaminetetraacetic acid (EDTA). *Mutation Research,* 115**,** 149-173.

HU, Y., LI, X., GENG, D., CAI, M., LI, R. & SUN, X. 2013. Influence of paper thickness on the electrochemical performances of graphene papers as an anode for lithium ion batteries. *Electrochimica Acta,* 91**,** 227-233.

HUANG, R., SHEN, Y., ZHAO, L. & YAN, M. 2012. Effect of hydrothermal temperature on structure and photochromic properties of WO_3 powder. *Advanced Powder Technology,* 23**,** 211-214.

HUIRACHE-ACUÑA, R., PARAGUAY-DELGADO, F., ALBITER, M., LARA-ROMERO, J. & MARTÍNEZ-SÁNCHEZ, R. 2009. Synthesis and characterization of WO_3 nanostructures prepared by an aged-hydrothermal method. *Materials characterization,* 60**,** 932-937.

HUMMERS, W. S. & OFFEMAN, R. E. 1958. Preparation of Graphitic Oxide. *Journal of the American Chemical Society,* 80**,** 1339-1339.

INFOPLEASE. 2014. *Sodium chloride* [Online]. Available: http://www.infoplease.com/encyclopedia/science/sodium-chloride-properties.html [Accessed June 11st 2014 2014].

JOHN M. HILLS, R. H. R., FRANK OSBORNE WOOD 2014. Salt (NaCl).

KOSTICK, D. S. 2014. *Sodium chloride* [Online]. Wikipedia. Available: http://en.wikipedia.org/wiki/Sodium_chloride [Accessed June 11st 2014 2014].

KUCINSKIS, G., BAJARS, G. & KLEPERIS, J. 2013. Graphene in lithium ion battery cathode materials: A review. *Journal of Power Sources,* 240**,** 66-79.

LANIGAN, R. S., YAMARIK, T. A. & ANDERSEN, F. A. 2002. Final report on the safety assessment of EDTA, calcium disodium EDTA, diammonium EDTA, dipotassium EDTA, disodium EDTA, TEA-EDTA, tetrasodium EDTA, tripotassium EDTA, trisodium EDTA, HEDTA, and trisodium HEDTA. *International Journal of Toxicology,* 21**,** 95-142.

LARCHER, D., BEATTIE, S., MORCRETTE, M., EDSTROEM, K., JUMAS, J.-C. & TARASCON, J.-M. 2007. Recent findings and prospects in the field of pure metals as negative electrodes for Li-ion batteries. *Journal of Materials Chemistry,* 17**,** 3759-3772.

LEE, C.-K., WANG, C.-C., LYU, M.-D., JUANG, L.-C., LIU, S.-S. & HUNG, S.-H. 2007. Effects of sodium content and calcination temperature on the morphology, structure and photocatalytic activity of nanotubular titanates. *Journal of colloid and interface science,* 316**,** 562-569.

LEE, W.-K., CHA, S.-H., KIM, K.-H., KIM, B.-W. & LEE, J.-C. 2009. Shape-controlled synthesis of gold icosahedra and nanoplates using Pluronic P123 block copolymer and sodium chloride. *Journal of Solid State Chemistry,* 182**,** 3243-3248.

LERF, A., HE, H., FORSTER, M. & KLINOWSKI, J. 1998. Structure of graphite oxide revisited. *The Journal of Physical Chemistry B,* 102**,** 4477-4482.

LI, D., MÜLLER, M. B., GILJE, S., KANER, R. B. & WALLACE, G. G. 2008. Processable aqueous dispersions of graphene nanosheets. *Nature nanotechnology,* 3**,** 101-105.

LI, W.-J. & FU, Z.-W. 2010. Nanostructured WO_3 thin film as a new anode material for lithium-ion batteries. *Applied Surface Science,* 256**,** 2447-2452.

LI, X., ZHANG, G., CHENG, F., GUO, B. & CHEN, J. 2006. Synthesis, characterization, and gas-sensor application of WO3 nanocuboids. *Journal of The Electrochemical Society,* 153**,** H133-H137.

LIDE, D. R. 2004. *CRC handbook of chemistry and physics*, CRC press.

LIU, B. & AYDIL, E. S. 2009. Growth of oriented single-crystalline rutile TiO_2 nanorods on transparent conducting substrates for dye-sensitized solar cells. *Journal of the American Chemical Society,* 131**,** 3985-3990.

LIU, Y., KANG, Z., CHEN, Z., SHAFIQ, I., ZAPIEN, J., BELLO, I., ZHANG, W. & LEE, S. 2009. Synthesis, characterization, and photocatalytic application of different ZnO nanostructures in array configurations. *Crystal Growth and Design,* 9**,** 3222-3227.

LONGER, M., ROBINSON, J. & GENNARO, A. 1990. Remington's Pharmaceutical Sciences. *by Gennaro AR, Mack Publishing Company, Easton, PA,* 1687.

LUO, F., JIA, C.-J., SONG, W., YOU, L.-P. & YAN, C.-H. 2005. Chelating ligand-mediated crystal growth of cerium orthovanadate. *Crystal growth & design,* 5**,** 137-142.

MARCANO, D. C., KOSYNKIN, D. V., BERLIN, J. M., SINITSKII, A., SUN, Z., SLESAREV, A., ALEMANY, L. B., LU, W. & TOUR, J. M. 2010. Improved synthesis of graphene oxide. *ACS nano,* 4**,** 4806-4814.

MCALLISTER, M. J., LI, J.-L., ADAMSON, D. H., SCHNIEPP, H. C., ABDALA, A. A., LIU, J., HERRERA-ALONSO, M., MILIUS, D. L., CAR, R. & PRUD'HOMME, R. K. 2007. Single sheet functionalized graphene by oxidation and thermal expansion of graphite. *Chemistry of Materials,* 19**,** 4396-4404.

MUNSHI, M. Z. A. 1995. *Handbook of Solid State Batteries & Capacitors*, World Scientific.

NOVOSELOV, K. S., GEIM, A. K., MOROZOV, S., JIANG, D., ZHANG, Y., DUBONOS, S., GRIGORIEVA, I. & FIRSOV, A. 2004. Electric field effect in atomically thin carbon films. *science,* 306**,** 666-669.

OBROVAC, M. & CHRISTENSEN, L. 2004. Structural changes in silicon anodes during lithium insertion/extraction. *Electrochemical and Solid-State Letters,* 7**,** A93-A96.

OHZUKU, T. & BRODD, R. J. 2007. An overview of positive-electrode materials for advanced lithium-ion batteries. *Journal of Power Sources,* 174**,** 449-456.

PEI, S. & CHENG, H.-M. 2012. The reduction of graphene oxide. *Carbon,* 50**,** 3210-3228.

PETERSON, A. A., VOGEL, F., LACHANCE, R. P., FRÖLING, M., ANTAL JR, M. J. & TESTER, J. W. 2008. Thermochemical biofuel production in hydrothermal media: a review of sub-and supercritical water technologies. *Energy & Environmental Science,* 1**,** 32-65.

POIZOT, P., LARUELLE, S., GRUGEON, S., DUPONT, L. & TARASCON, J. 2000. Nano-sized transition-metal oxides as negative-electrode materials for lithium-ion batteries. *Nature,* 407**,** 496-499.

RAI, A. K., GIM, J., ANH, L. T. & KIM, J. 2013a. Partially reduced Co3O4/graphene nanocomposite as an anode material for secondary lithium ion battery. *Electrochimica Acta,* 100**,** 63-71.

RAI, A. K., GIM, J., ANH, L. T. & KIM, J. 2013b. Partially reduced Co_3O_4/graphene nanocomposite as an anode material for secondary lithium ion battery. *Electrochimica Acta,* 100**,** 63-71.

RAI, A. K., GIM, J., SONG, J., MATHEW, V., ANH, L. T. & KIM, J. 2012. Electrochemical and safety characteristics of TiP_2O_7–graphene nanocomposite anode for rechargeable lithium-ion batteries. *Electrochimica Acta,* 75**,** 247-253.

RAO, F., ZHOU, Y., LI, T. & WANG, Y. 2009. Synthesis of radially aligned single-walled carbon nanotubes on a SiO_2/Si substrate by introducing sodium chloride. *Carbon,* 47**,** 2548-2552.

ROMANÍ, A., GARROTE, G., ALONSO, J. L. & PARAJÓ, J. C. 2010. Bioethanol production from hydrothermally pretreated *Eucalyptus globulus*wood. *Bioresource technology,* 101**,** 8706-8712.

SAQUY, P. C., MAIA CAMPOS, G., SOUSA NETO, M. D., GUIMARÃES, L. F. & PÉCORA, J. D. 1994. Evaluation of chelating action of EDTA in association with Dakin's solution. *Brazilian dental journal,* 5**,** 65-70.

SARON, K. & HASHIM, M. 2013. Broad visible emission from GaN nanowires grown on n-Si (111) substrate by PVD for solar cell application. *Superlattices and Microstructures,* 56**,** 55-63.

SASIDHARAN, M., GUNAWARDHANA, N., YOSHIO, M. & NAKASHIMA, K. 2012. WO_3hollow nanospheres for high-lithium storage capacity and good cyclability. *Nano Energy,* 1**,** 503-508.

SAYıLKAN, F., ERDEMOĞLU, S., ASILTÜRK, M., AKARSU, M., ŞENER, Ş., SAYıLKAN, H., ERDEMOĞLU, M. & ARPAÇ, E. 2006. Photocatalytic performance of pure anatase nanocrystallite TiO_2 synthesized under low temperature hydrothermal conditions. *Materials research bulletin,* 41**,** 2276-2285.

SCHNIEPP, H. C., LI, J.-L., MCALLISTER, M. J., SAI, H., HERRERA-ALONSO, M., ADAMSON, D. H., PRUD'HOMME, R. K., CAR, R., SAVILLE, D. A. & AKSAY, I. A. 2006. Functionalized single graphene sheets derived from splitting graphite oxide. *The Journal of Physical Chemistry B,* 110**,** 8535-8539.

SCHULTZ, B. J., PATRIDGE, C. J., LEE, V., JAYE, C., LYSAGHT, P. S., SMITH, C., BARNETT, J., FISCHER, D. A., PRENDERGAST, D. & BANERJEE, S. 2011. Imaging local electronic corrugations and doped regions in graphene. *Nature communications,* 2**,** 372.

SHIN, H. J., KIM, K. K., BENAYAD, A., YOON, S. M., PARK, H. K., JUNG, I. S., JIN, M. H., JEONG, H. K., KIM, J. M. & CHOI, J. Y. 2009. Efficient reduction of graphite oxide by sodium borohydride and its effect on electrical conductance. *Advanced Functional Materials,* 19**,** 1987-1992.

SHIVA, K., RAMAKRISHNA MATTE, H., RAJENDRA, H., BHATTACHARYYA, A. J. & RAO, C. 2013. Employing synergistic interactions between few-layer WS_2 and reduced graphene oxide to improve lithium storage, cyclability and rate capability of Li-ion batteries. *Nano Energy,* 2**,** 787-793.

SHUKLA, A. & PREM KUMAR, T. 2013. Nanostructured electrode materials for electrochemical energy storage and conversion. *Wiley Interdisciplinary Reviews: Energy and Environment,* 2**,** 14-30.

SICILIANO, T., TEPORE, A., MICOCCI, G., SERRA, A., MANNO, D. & FILIPPO, E. 2008. WO_3 gas sensors prepared by thermal oxidization of tungsten. *Sensors and Actuators B: Chemical,* 133**,** 321-326.

SONG, P., ZHANG, X., SUN, M., CUI, X. & LIN, Y. 2012. Graphene oxide modified TiO_2 nanotube arrays: enhanced visible light photoelectrochemical properties. *Nanoscale,* 4**,** 1800-1804.

SUPOTHINA, S., SEEHARAJ, P., YORIYA, S. & SRIYUDTHSAK, M. 2007. Synthesis of tungsten oxide nanoparticles by acid precipitation method. *Ceramics International,* 33**,** 931-936.

TAO, H.-C., FAN, L.-Z., YAN, X. & QU, X. 2012. In situ synthesis of TiO_2–graphene nanosheets composites as anode materials for high-power lithium ion batteries. *Electrochimica Acta,* 69**,** 328-333.

ULLMANN, F. & ELVERS, B. 1991. *Encyclopedia of industrial chemistry*, VCH.

VAYSSIERES, L., CHANÉAC, C., TRONC, E. & JOLIVET, J. P. 1998. Size tailoring of magnetite particles formed by aqueous precipitation: An example of thermodynamic stability of nanometric oxide particles. *Journal of colloid and interface science,* 205**,** 205-212.

WANG, J., XU, Y., HOJAMBERDIEV, M., PENG, J. & ZHU, G. 2009. Na2EDTA-assisted hydrothermal synthesis and luminescent properties of YVO4: Eu3+ with different morphologies in a wide pH range. *Materials science & engineering. B, Solid-state materials for advanced technology,* 156**,** 42-47.

WANG, X., LI, B., LIU, D. & XIONG, H. 2014. $ZnWO_4$ nanocrystals/reduced graphene oxide hybrids: Synthesis and their application for Li ion batteries. *Science China Chemistry,* 57**,** 122-126.

WINTTERLIN, J. & BOCQUET, M.-L. 2009. Graphene on metal surfaces. *Surface Science,* 603**,** 1841-1852.

WOLCOTT, A., KUYKENDALL, T. R., CHEN, W., CHEN, S. & ZHANG, J. Z. 2006. Synthesis and characterization of ultrathin WO_3 nanodisks utilizing long-chain poly (ethylene glycol). *The Journal of Physical Chemistry B,* 110**,** 25288-25296.

XIAO, W., WANG, Z., GUO, H., LI, X., WANG, J., HUANG, S. & GAN, L. 2013. Fe_2O_3 particles enwrapped by graphene with excellent cyclability and rate capability as anode materials for lithium ion batteries. *Applied Surface Science,* 266**,** 148-154.

XU, R. & ZENG, H. C. 2003. Mechanistic investigation on salt-mediated formation of free-standing Co_3O_4 nanocubes at 95^{o}C. *The Journal of Physical Chemistry B,* 107**,** 926-930.

XU, Z., KANG, X., LI, C., HOU, Z., ZHANG, C., YANG, D., LI, G. & LIN, J. 2010. Ln^{3+} (Ln= Eu, Dy, Sm, and Er) ion-doped YVO4 nano/microcrystals with multiform morphologies: Hydrothermal synthesis, growing mechanism, and luminescent properties. *Inorganic chemistry,* 49**,** 6706-6715.

YANG, H., SONG, T., LEE, S., HAN, H., XIA, F., DEVADOSS, A., SIGMUND, W. & PAIK, U. 2013a. Tin indium oxide/graphene nanosheet nanocomposite as an anode material for lithium ion batteries with enhanced lithium storage capacity and rate capability. *Electrochimica Acta,* 91**,** 275-281.

YANG, Q., LU, Z., LIU, J., LEI, X., CHANG, Z., LUO, L. & SUN, X. 2013b. Metal oxide and hydroxide nanoarrays: Hydrothermal synthesis and applications as supercapacitors and nanocatalysts. *Progress in Natural Science: Materials International,* 23**,** 351-366.

YANG, X., ZHOU, L., CHEN, C. & XU, J. 2010. Synthesis of Zr-MCM-41 by the assistance of sodium chloride in the self-generated acid conditions. *Materials Chemistry and Physics,* 120**,** 42-45.

YIN, J., CAO, H., ZHANG, J., QU, M. & ZHOU, Z. 2012. Synthesis and Applications of γ-Tungsten Oxide Hierarchical Nanostructures. *Crystal Growth & Design,* 13**,** 759-769.

YOON, S., JO, C., NOH, S. Y., LEE, C. W., SONG, J. H. & LEE, J. 2011. Development of a high-performance anode for lithium ion batteries using novel ordered mesoporous tungsten oxide materials with high electrical conductivity. *Physical Chemistry Chemical Physics,* 13**,** 11060-11066.

YU, M., SUN, H., SUN, X., LU, F., HU, T., WANG, G., QIU, H. & LIAN, J. 2013. 3D WO3 nanowires/graphene nanocomposite with improved reversible capacity and cyclic stability for lithium ion batteries. *Materials Letters,* 108**,** 29-32.

ZHENG, F., ZHANG, M. & GUO, M. 2013. Controllable preparation of WO_3 nanorod arrays by hydrothermal method. *Thin Solid Films,* 534**,** 45-53.

(This page is empty deliberately)

BIOGRAPHY

Augus Tino Tri Widyantoro obtained his B.Sc. in Materials and Metallurgical Engineering from Sepuluh Nopember Institute of Technology in Indonesia (ITS Surabaya) at 2013, under the supervision of Diah Susanti, Ph.D, with a thesis on "The Effect of Calcination Temperature on the Morphology and Electrochemical Properties of WO_3 as Electrode Materials for Pseudocapacitor".

Currently, He is completing his Dual Master Degree in Materials Science and Engineering, National Taiwan University of Science and Technology (NTUST) and Materials and Metallurgical Engineering, ITS under the supervision of Professor Chen-Hao Wang, Prof. Bing-Joe Hwang, Dr. Ming-Yao Cheng and Diah Susanti Ph. D, with a thesis addressed to the preparation and characterization of WO_3 as anode material for lithium ion battery.